Structured Illumination Microscopy with X-rays

Zachary Laker
March 2014

PHAS3400: Physics Project BSc
First Supervisor: Professor Ian Robinson
Second Supervisor: Dr Graeme Morrison

Abstract

Structured illumination microscopy (SIM) is a well-established optical imaging technique allowing the optical sectioning of thick samples using a two-dimensional microscope setup. The technique has been well demonstrated using optical wavelengths and is beneficial as a 3D imaging technique due, in part, to the low cost and ease of conversion of 2D microscope setups to image in a SIM mode. Such a technique may be extended theoretically to encompass X-ray wavelength imaging, representative of SIM imaging with a transmission X-ray microscope (TXM), but no major literature to date has provided an attempt at such a method of TXM imaging. A computational model of the TWIN-MIC TXM/STXM facility, located at the Elettra synchrotron in Italy, was constructed, with simulation results confirming the ability of such a TXM to operate in a SIM mode. Several requirements to facilitate such a mode of imaging were investigated and verified, including the need for a highly incoherent illumination source. Experiments carried out at TWIN-MIC to verify such computational results in December 2013 proved inconclusive, with experiments at the facility in May 2014 expected to yield more successful results.

Contents

1. Introduction

1.1 Overview

It is common in microscopic studies of thick samples such as a biological specimen to stain the specimen and then, using an apparatus such as the microtome, to cut the sample into extraordinarily thin slices for imaging using 2D microscopy techniques [1]. Such an imaging process is undesirable as the specimen is viewed in an unnatural state. Alternatively, if thick slices or whole-mounts are examined, interior structures within the specimen may be masked by interference from structures either side of the focal plane [2].

Focal planes located deep within a thick sample may be imaged clearly through a process referred to as optical sectioning, requiring a microscope of suitable design. Such imaging techniques necessarily achieve depth resolution, allowing the three dimensional reconstruction of a sample from a collection, or series, of images captured at different focal planes, as depicted in figure 1.1. Several different techniques are capable of achieving optical sectioning, with each providing varying degrees of quality in sectioned images [3]. The issues involved with the physical sectioning of a thick sample to gain depth resolution, or alternatively, imaging a thick sample naturally but with no rejection of out-of-focus light from planes bordering the focal plane, provides a clear demonstration of the merit of optical sectioning techniques. Optical sectioning of thick samples has been the subject of much literature published in the field of microscopy ([2]; [3]; [4]; [5]; [6]), with several approaches taken involving a variety of microscope setups, particularly confocal ([6]; [7]; [8]; [9]). An alternative type of microscopy with the potential capability of optically sectioning a sample is structured illumination microscopy (SIM).

The image generated in a conventional wide-field microscope attenuates all but the zero spatial frequency with defocus in the system transfer function [2], [11]. Hence, the central motivation of the initial SIM studies involved modification of the illumination system of the microscope with the desire of projecting a single-spatial-frequency grid pattern onto the imaged object, such that the system might image efficiently only the in-focus portion of the object [12], [13]. Consequently, SIM presents a method by which depth, or ‘axial’, resolution can be achieved as, by adjusting the axial position of the focal plane of the optical system, the images of the sample obtained correspond to optical sections of the sample at different depths [2], with out-of-focus signals of the object well attenuated by the system transfer function. Combined, these optical sections form a magnified three dimensional image of the sample, with magnification arising due to the magnification properties of the optical system [2].

Additional processing is required in order to remove the illumination pattern from the final image; analysis of the final image is hindered due to the illumination pattern modulating the image signal [2]. Such processing algorithms allow the removal of the illumination grid pattern from the final image; optically sectioned images taken from a conventional microscope may be obtained without the illumination pattern present [2]. SIM offers a more economical alternative to other depth resolution techniques, in particular confocal microscopy, providing similar achievable resolutions [8]. The advantage of SIM over confocal microscopy techniques, however, is that it may be utilised on a wide-field microscope with only minor modifications required, as it does not involve a scanning device [8]. A key reflection on the main body of SIM literature was the restriction to only optical wavelength sources used in experiments, giving maximum microscope resolution limits of the order hundreds of nanometres. A possible extension to the field of SIM, with a focus on optical sectioning, would be the extension to shorter wavelength domains, particularly to soft X-ray level (10nm – 0.1nm), with necessary gains in resolution.

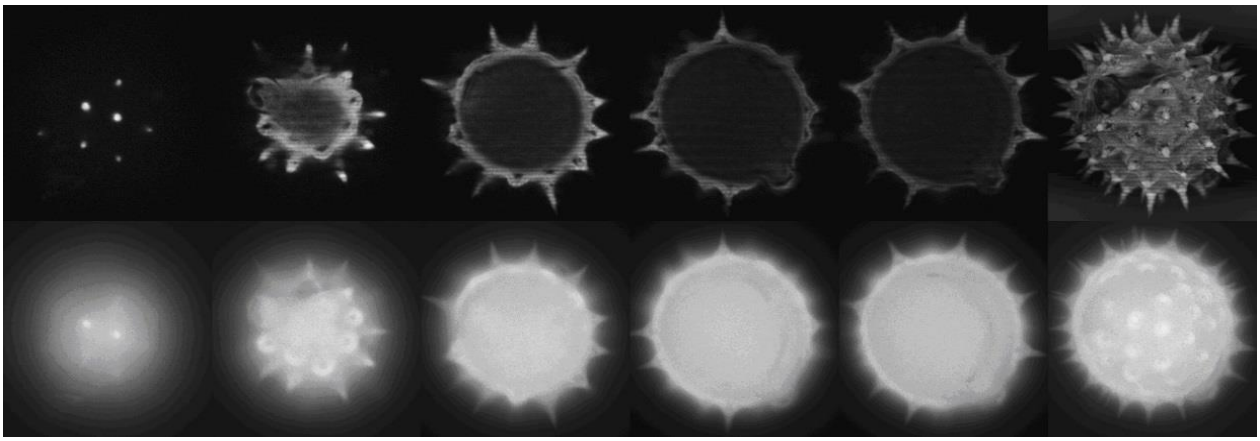

Figure 1.1: Demonstration of optical sectioning of a birch pollen grain [14]. Upper row gives successive focal series images with fringe pattern removed, although some artefacts are still present. Bottom row gives successive focal series images using conventional uniform illumination. Final column gives reconstructed 3D images using focal series images for each row.

Soft X-rays have been utilised in various imaging techniques to allow much greater resolution of images to be achieved than possible with optical light, and of imaging of samples too thick to be viewed by electron microscopy such as chromosomes and other biological specimens [15]. As such, the author was presented with the task of computationally simulating such a mode of imaging using an X-ray microscope. The transmission X-ray microscope (TXM) of choice was the twin-microscope (TWIN-MIC) TXM. The TWIN-MIC facility is located at the Elettra synchrotron source near Trieste, Italy. Such a choice was made due to both the close affiliation between the author's research group and the facility, and because the research group had scheduled beam time for December 2013 and May 2014 at TWIN-MIC, whereby such a mode of imaging with a TXM would be attempted experimentally.

For the author's part, a model using the TWIN-MIC setup parameters was to be constructed in a suitable programming language or numerical development environment (NDE). Once a working simulation was demonstrated, such a model would then provide close support for experiments, with the potential of carrying out on-the-spot simulations in order to compare against experimental results. In addition, the author was to provide support and expertise during such experimental visits.

The task required much provisional study of related topics, in particular, a thorough overview of Fourier optics theory, in order to facilitate the correct modelling of such a system. In addition, a comprehensive overview of related X-ray imaging literature was carried out. As such, the author's report is inherently multi-faceted. The author will seek to guide the reader briefly through a section of introductory theory, followed by some rudimentary simulation results. Successive chapters will seek to establish a more robust model, introducing some additional, more complex theory, in order to facilitate a more vigorous and robust simulation. Once a complete model is established, the author will briefly discuss preliminary experimental attempts carried out during the December 2013 visit to TWIN-MIC, followed by a period of discussion and some concluding statements. Finally, all supporting documents will be provided in a list of references, with the complete simulation code given in an additional appendix. For more information on the field of X-ray imaging and optics the reader is directed to the further reading section of the report where an ample list of supporting documents and texts is provided.

1.2 Simulation Details

The simulations carried out for this task were constructed within the Mathworks MATLAB® NDE (Release version 2010a) using a Samsung Electronics machine, specifications: Intel® Core™ i7-3630QM quad-core CPU 2.40GHz rate, 8.00Gb installed memory (RAM), 64-bit Operating System with x64-based processor. The choice of NDE was primarily due to MATLAB's combination of superior array handling capabilities, graphical manipulation and plotting tools and ease of use. Figures were written

to file (PDF) using a user-submitted export script [16], whilst figures themselves adhered to the *jet* false-colour map format, as depicted in figure 1.2. The complete model code is included in Appendix 1, with supplementary image objects used in the code provided as attachments to the electronic copy of the report.

Figure 1.2: Normalised false colour *jet* map utilised in subsequent figures

1.3 Mathematical Conventions

In order to arrive at the necessary theoretical results to achieve SIM, we must first familiarise ourselves with several key optical theories, with particular focus on those necessary results from Fourier optics theory. In addition, we must introduce ourselves to several X-ray imaging theories, investigating the necessary modifications required to the standard optical theory we will derive when working with X-ray wavelengths.

Throughout our investigation we will work within a Cartesian co-ordinate basis, unless otherwise stated. Thus, an arbitrary point (r_x, r_y, r_z) in space may be represented by the vector:

$$\boldsymbol{r} = r_x\hat{\boldsymbol{e}}_{\boldsymbol{x}} + r_y\hat{\boldsymbol{e}}_{\boldsymbol{y}} + r_z\hat{\boldsymbol{e}}_{\boldsymbol{z}} \tag{1.1}$$

Here, the vector is indicated by the bold typeface and $\hat{\boldsymbol{e}}_{\boldsymbol{x}}$, $\hat{\boldsymbol{e}}_{\boldsymbol{y}}$ and $\hat{\boldsymbol{e}}_{\boldsymbol{z}}$ are the Cartesian unit vectors, forming a complete orthonormal basis set. We will also encounter on several occasions a number of Fourier transforms and Fourier transform theorems, and as such they are introduced here to clarify variable conventions adopted. The Fourier transform convention embraced is:

$$\mathcal{F}(\boldsymbol{q}) = \int_{-\infty}^{\infty}\int_{-\infty}^{\infty}\int_{-\infty}^{\infty} F(\boldsymbol{r})e^{-i2\pi\boldsymbol{q}\cdot\boldsymbol{r}}d^3\boldsymbol{r} \tag{1.2}$$

$$F(\boldsymbol{r}) = \int_{-\infty}^{\infty}\int_{-\infty}^{\infty}\int_{-\infty}^{\infty} \mathcal{F}(\boldsymbol{q})e^{i2\pi\boldsymbol{q}\cdot\boldsymbol{r}}d^3\boldsymbol{q} \tag{1.3}$$

where $\boldsymbol{q}\cdot\boldsymbol{r} = q_xr_x + q_yr_y + q_zr_z$, $d^3\boldsymbol{r} = dxdydz$, $d^3\boldsymbol{q} = dq_xdq_ydq_z$ and F is some arbitrary function. For simplicity, when referring to (1.2) and (1.3) only a single integration sign will be used for representation of the transform. In addition, we note that if $\boldsymbol{r}$ has units m, then $\boldsymbol{q}$ must have units of m^{-1}, in order to keep the exponent dimensionless.

We also introduce here two important Fourier transform theorems. Firstly, the convolution theorem [17]. The convolution theorem is defined by:

$$[H \otimes F]_{\boldsymbol{r}} = \int_{-\infty}^{\infty} H(\boldsymbol{r}')F(\boldsymbol{r}-\boldsymbol{r}')\,d^3\boldsymbol{r}' = \int_{-\infty}^{\infty} H(\boldsymbol{r}-\boldsymbol{r}')F(\boldsymbol{r}')\,d^3\boldsymbol{r}' \tag{1.4}$$

where $\boldsymbol{r}-\boldsymbol{r}' = (r_x - r_x', r_y - r_y', r_z - r_z')$. The convolution theorem states that:

$$FT\{[H \otimes F]_{\boldsymbol{r}}\} = \mathcal{H}(\boldsymbol{q})\mathcal{F}(\boldsymbol{q}) \tag{1.5}$$

where FT indicates a Fourier transform is taken, and $\mathcal{H}$, $\mathcal{F}$ represent the Fourier transforms of H and F, respectively. The convolution theorem may thus be stated explicitly: The Fourier transform of the convolution between two functions is equal to the product of the Fourier transforms of each of the functions involved in the convolution. Finally, we state Parseval's theorem [17]:

$$\int_{-\infty}^{\infty} |F(\boldsymbol{r})|^2\,d^3\boldsymbol{r} = \int_{-\infty}^{\infty} |\mathcal{F}(\boldsymbol{q})|^2\,d^3\boldsymbol{q} \tag{1.6}$$

2. Fundamental Optical Theory

2.1 Coherent Field Propagation:

We begin our overview with the introduction of a time- and space- varying electromagnetic source field, which in the most general case may be described as a vector field:

$$\boldsymbol{E}(\boldsymbol{r},t) = E_x(\boldsymbol{r},t)\hat{\boldsymbol{e}}_{\boldsymbol{x}} + E_y(\boldsymbol{r},t)\hat{\boldsymbol{e}}_{\boldsymbol{y}} + E_z(\boldsymbol{r},t)\hat{\boldsymbol{e}}_{\boldsymbol{z}} \tag{2.1}$$

During our investigation, we will be studying the field distributions in the 2D ($\hat{\boldsymbol{e}}_{\boldsymbol{x}}, \hat{\boldsymbol{e}}_{\boldsymbol{y}}$) plane, with the planes located at various axial distances z from a set origin, allowing the field distribution to propagate in the $\hat{\boldsymbol{e}}_{\boldsymbol{z}}$ direction. We may introduce a vector defining the 2D ($\hat{\boldsymbol{e}}_{\boldsymbol{x}}, \hat{\boldsymbol{e}}_{\boldsymbol{y}}$) plane $\boldsymbol{\rho} = r_x\hat{\boldsymbol{e}}_{\boldsymbol{x}} + r_y\hat{\boldsymbol{e}}_{\boldsymbol{y}}$ and define the field at an arbitrary plane as:

$$\boldsymbol{E}(\boldsymbol{\rho},z,t) = E_x(\boldsymbol{\rho},z,t)\hat{\boldsymbol{e}}_{\boldsymbol{x}} + E_y(\boldsymbol{\rho},z,t)\hat{\boldsymbol{e}}_{\boldsymbol{y}} \tag{2.2}$$

where we have removed the $\hat{\boldsymbol{e}}_{\boldsymbol{z}}$ component of the field as this will not be of interest during our investigation. Maxwell's equations of classical electrodynamics [18] govern the evolution of this field. When solving for a single field component, particular focus is given to the inhomogeneous scalar, time-dependent wave equation obtained [19]:

$$\left(\nabla^2 - \frac{n^2}{c^2}\frac{\partial^2}{\partial t^2}\right)E(x,t) = -S(x,t) \tag{2.3}$$

where c is the speed of light in a vacuum, n is the system medium refractive index and $S(x,t)$ corresponds to the physical source of the field component. For a coherent illumination source, the single-component electromagnetic field and source field may be separated into a product of time-dependent and spatial-dependent functions [19]. The time-dependent field components take the form of a harmonic wave, represented by a complex exponential time-dependent phase:

$$E(x,t) = E(x)e^{-i\omega t} \tag{2.4}$$

$$S(x,t) = S(x)e^{-i\omega t} \tag{2.5}$$

where $\omega = 2\pi kc$ is the angular frequency and $k = 1/\lambda$ is the wavenumber for the system in vacuum. Equations (2.4) and (2.5) may be substituted into (2.3), leading directly to the Helmholtz equation [19]:

$$\left(\nabla^2 - \left(\frac{2n\pi}{\lambda}\right)^2\right)E(x) = -S(x) \tag{2.6}$$

Equation (2.6) serves as the basis of the light propagation theory we will utilise in our investigation. Developing the theory further, we introduce a set of the Kirchhoff's boundary conditions [20]:

- The field at $z = 0$ is bounded by a finite aperture
- The field inside the aperture is unaffected by the presence of the aperture

Figure 2.1 depicts the field $\boldsymbol{E}(\boldsymbol{\rho_1},z)$ resulting from the propagation of the aperture based field $\boldsymbol{E}(\boldsymbol{\rho}_0,0)$. The propagation is formally presented in the case of scalar fields [21] and vector fields [22], with the scalar field relation between $E(\boldsymbol{\rho_1},z)$ and $E(\boldsymbol{\rho}_0,0)$ found to be:

$$E(\boldsymbol{\rho_1},z) = -ik\int_{-\infty}^{\infty} E(\boldsymbol{\rho}_0,0)\left(1 - \frac{1}{i2\pi kR}\right)\frac{e^{i2\pi kR}}{R}\cos(\theta)\,d^2\boldsymbol{\rho}_0 \tag{2.7}$$

where $R = |\boldsymbol{r}_1 - \boldsymbol{r}_0| = (|\boldsymbol{\rho_1} - \boldsymbol{\rho_0}|^2 + z^2)^{1/2}$ and $\cos(\theta) = z/R$, as shown in figure 2.1. Equation (2.7) is known as the Rayleigh-Sommerfeld diffraction integral and can be formally expressed as a 2D convolution [19]:

$$E(\boldsymbol{\rho}, z) = [H(\boldsymbol{\rho}, z) \otimes E(\boldsymbol{\rho}, 0)]_{\boldsymbol{\rho}} \tag{2.8}$$

where we have introduced:

$$H(\boldsymbol{\rho}, z) = -ik\frac{z}{\boldsymbol{\rho}^2 + z^2}e^{i2\pi k(\boldsymbol{\rho}^2+z^2)^{\frac{1}{2}}}\left(1 + \frac{i}{2\pi k(\boldsymbol{\rho}^2 + z^2)^{\frac{1}{2}}}\right) \tag{2.9}$$

and the subscript $\boldsymbol{\rho}$ in (2.8) denotes the convolution variable.

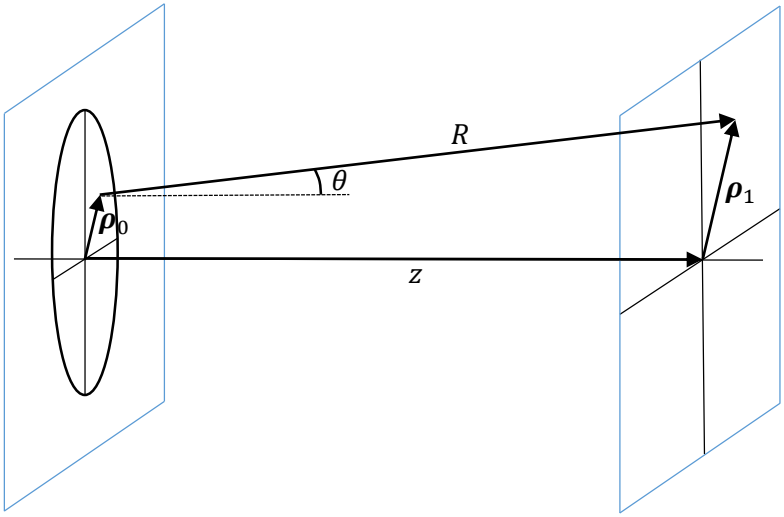

Figure 2.1: Field propagation geometry describing the Kirchhoff boundary conditions.

$H(\boldsymbol{\rho}, z)$ represents a response function, propagating the field through free space between axial planes separated by an axial distance z. Hence, $H(\boldsymbol{\rho}, z)$ is referred to as the Rayleigh-Sommerfeld free-space propagator. Equation (2.8) translates into a product in the frequency domain upon utilisation of the convolution theorem (1.5) [23]:

$$\mathcal{E}(\boldsymbol{q}; z) = \mathcal{H}(\boldsymbol{q}; z)\mathcal{E}(\boldsymbol{q}; 0) \tag{2.10}$$

where, $\mathcal{H}(\boldsymbol{q}; z)$ is the Fourier transform of the Rayleigh-Sommerfeld free-space propagator (2.9):

$$\mathcal{H}(\boldsymbol{q}; z) = \int_{-\infty}^{\infty} H(\boldsymbol{\rho}, z)e^{-i2\pi\boldsymbol{q}\cdot\boldsymbol{\rho}}d^2\boldsymbol{\rho} \tag{2.11}$$

and $\mathcal{E}(\boldsymbol{q}; z)$ is the Fourier transform of the field distribution:

$$\mathcal{E}(\boldsymbol{q}; z) = \int_{-\infty}^{\infty} E(\boldsymbol{\rho}, z)e^{-i2\pi\boldsymbol{q}\cdot\boldsymbol{\rho}}d^2\boldsymbol{\rho} \tag{2.12}$$

Evaluation of (2.11) leads to the result [23]:

$$\mathcal{H}(\boldsymbol{q}; z) = e^{\pm i2\pi z\left(k^2 - \boldsymbol{q}^2\right)^{1/2}} \tag{2.13}$$

The dual sign in the sign of the exponent of (2.13) allows for the possibility of the field propagation in both the $+z$ and $-z$ directions, which is a possibility, provided that the field source is located outside the region between the planes of interest. As we will see in due course, this plays an important role in 3D imaging.

The radiative approximation ($kR \gg 1$) [19] may be applied to the Rayleigh-Sommerfield diffraction integral (2.7) as we are restricting ourselves to the case of radiative fields, simplifying it to:

$$E(\boldsymbol{\rho}_1, z) = -ik\int_{-\infty}^{\infty} E(\boldsymbol{\rho}_0, 0)\frac{e^{i2\pi kR}}{R}cos\theta d^2\boldsymbol{\rho}_0 \tag{2.14}$$

From (2.14) we note that, in a homogeneous medium, a spherical wave of the form $e^{i2\pi kR}/R$ emanates from a harmonically oscillating point source [18]. Hence, as illustrated in figure 2.2, the radiative field may be considered as a superposition of spherical waves, known as Huygens wavelets, originating from the source plane [19]. Each point in the source plane acts as a virtual point source of wavelets whose amplitude is proportional to that of the source field, weighted by a factor $\cos\theta$.

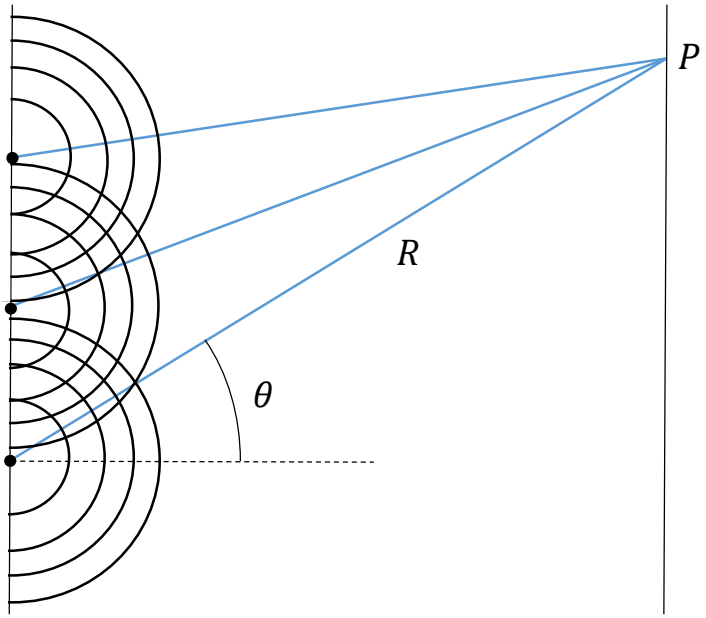

Figure 2.2: Demonstration of formation of radiative field through superposition of Huygens wavelets.

A small-angle approximation may be applied to (2.14), known as the paraxial approximation, which amounts to the conditions $\cos\theta \to 1$ and $R \to z$ [19]. This approximation may be applied as, for most applications, the wavefronts associated with the fields propagating from one plane to another vary in the transverse direction slowly, equivalent to the wavefronts deviating only weakly from the axial propagation direction. We thus obtain [23]:

$$E(\boldsymbol{\rho}_1, z) = -\frac{ik}{z}\int_{-\infty}^{\infty} E(\boldsymbol{\rho}_0, 0)e^{i2\pi kR}d^2\boldsymbol{\rho}_0 \tag{2.15}$$

The paraxial approximation may be relaxed further by using a Taylor expansion of the term R. From simple geometry:

$$R = (z^2 + (\boldsymbol{\rho}_1 - \boldsymbol{\rho}_0)^2)^{\frac{1}{2}} = z\left(1 + \left(\frac{\boldsymbol{\rho}_1 - \boldsymbol{\rho}_0}{z}\right)^2\right)^{\frac{1}{2}} \tag{2.16}$$

and, upon expanding to second order, we obtain:

$$R = z\left(1 + \frac{1}{2}\left(\frac{\boldsymbol{\rho}_1 - \boldsymbol{\rho}_0}{z}\right)^2 + \cdots\right) \to z + \frac{(\boldsymbol{\rho}_1 - \boldsymbol{\rho}_0)^2}{2z} \tag{2.17}$$

Valid when $(\boldsymbol{\rho}_1 - \boldsymbol{\rho}_0)^4 \ll \lambda z^3$, this restrained approximation is called the Fresnel approximation [23]. Applying to (2.15), we obtain:

$$E(\boldsymbol{\rho}_1, z) = -\frac{ik}{z}e^{i2\pi kz}\int_{-\infty}^{\infty} E(\boldsymbol{\rho}_0, 0)e^{\frac{i\pi k}{z}(\boldsymbol{\rho}_1 - \boldsymbol{\rho}_0)^2}d^2\boldsymbol{\rho}_0 \tag{2.18}$$

This is the well-known Fresnel diffraction integral [23]. Expanding the quadratic exponent term, we acquire a more convenient form of the Fresnel diffraction integral:

$$E(\boldsymbol{\rho}_1, z) = -\frac{ik}{z} e^{i2\pi kz} e^{\frac{i\pi k}{z}\boldsymbol{\rho}_1{}^2} \int_{-\infty}^{\infty} E(\boldsymbol{\rho}_0, 0) e^{-\frac{2i\pi k}{z}\boldsymbol{\rho}_1 \cdot \boldsymbol{\rho}_0} e^{\frac{i\pi k}{z}\boldsymbol{\rho}_0{}^2} d^2\boldsymbol{\rho}_0 \tag{2.19}$$

This may be recast in a similar vain to the Rayleigh-Somerfeld diffraction integral convolution result (2.8) dealt with above, where the Fresnel free-space propagator is defined to be:

$$H(\boldsymbol{\rho}, z)_{Fresnel} = -\frac{ik}{z} e^{i2\pi kz} e^{\frac{i\pi k}{z}\boldsymbol{\rho}^2} \tag{2.20}$$

Translating to the frequency domain we may realise the Fresnel approximation as the condition $\boldsymbol{q}^2 \ll k^2$, allowing (2.13) to be re-expressed in the form of (2.10) using the substitution:

$$(k^2 - \boldsymbol{q}^2)^{\frac{1}{2}} \to k\left(1 - \frac{\boldsymbol{q}^2}{2k^2}\right)$$

where the mixed representation of the free-space Fresnel propagator is given by [23]:

$$\mathcal{H}(\boldsymbol{q}, z)_{Fresnel} = e^{i2\pi kz} e^{\frac{-i\pi z}{k}\boldsymbol{q}^2} \tag{2.21}$$

Again, by construction, $H(\boldsymbol{\rho}, z)_{Fresnel}$ and $\mathcal{H}(\boldsymbol{q}, z)_{Fresnel}$ are Fourier transform pairs.

We may note here that there exist multiple other optical domains of approximation bordering the Fresnel region, whereby the small-angle Fresnel approximation is not valid. These consist of the Paraxial-Fraunhofer and Fraunhofer regimes respectively, which are utilised for systems consisting of larger propagation distances than the Fresnel regime [16]. The system that will be the central focus of this report operates only within the domain of the Fresnel regime, as we will soon demonstrate, and so the theory utilised for the Paraxial-Fraunhofer and Fraunhofer regimes will not be discussed here.

2.2 Coherent Imaging with a lens:

We may proceed in discussing the effects of a lens, free from aberrations (i.e. a perfect lens), upon a propagating field. The field transmission of a perfect thin lens is defined by [19]:

$$t(\boldsymbol{\rho}) = P(\boldsymbol{\rho}) e^{-\frac{i\pi k}{f}\boldsymbol{\rho}^2} \tag{2.22}$$

where $P(\boldsymbol{\rho})$ is a pupil function. In effect, the lens adds a quadratically varying phase to the propagating field. An additional fixed phase shift is imparted on the propagating field due to the lens thickness, but this may be ignored as it plays no role in imaging. Continuing, we consider the imaging geometry shown in figure 2.3, where a field propagates from a plane $\boldsymbol{\rho}_0$ to a plane $\boldsymbol{\rho}_2$ via a lens located at an intermediate plane $\boldsymbol{\rho}_1$.

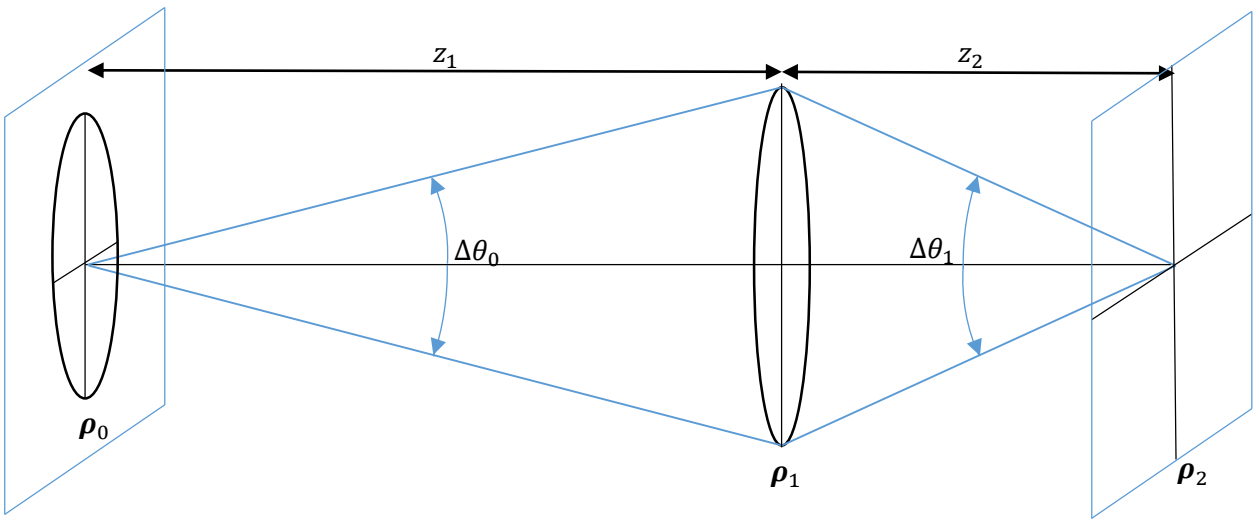

Figure 2.3: Diagram of optical lens system used to generate an image of an illuminated object.

We proceed by deriving the field incident on the lens at the lens plane, which is readily achieved with use of the Fresnel approximation (2.20):

$$E_{-}(\boldsymbol{\rho}_1) = \frac{-ik}{z_1} e^{i2\pi k z_1} \int_{-\infty}^{\infty} E(\boldsymbol{\rho}_0) e^{\frac{i\pi k}{z_1}(\boldsymbol{\rho}_1 - \boldsymbol{\rho}_0)^2} d^2\boldsymbol{\rho}_0 \tag{2.23}$$

where the negative subscript indicates the field prior to propagating through the lens and, for purposes of brevity, the notational convention $E(\boldsymbol{\rho}_0, z_0) = E(\boldsymbol{\rho}_0)$ has been adopted. The field emerging right of the lens is then $E_{+}(\boldsymbol{\rho}_1) = t(\boldsymbol{\rho}_1) E_{-}(\boldsymbol{\rho}_1)$, which, utilising (2.22) and (2.23), is:

$$E_{+}(\boldsymbol{\rho}_1) = \frac{-ik}{z_1} e^{i2\pi k z_1} \int_{-\infty}^{\infty} E(\boldsymbol{\rho}_0) P(\boldsymbol{\rho}_1) e^{\frac{i\pi k}{f}{\boldsymbol{\rho}_1}^2} e^{\frac{i\pi k}{z_1}(\boldsymbol{\rho}_1 - \boldsymbol{\rho}_0)^2} d^2\boldsymbol{\rho}_0 \tag{2.24}$$

Expanding the quadratic terms of (2.24) leads to:

$$E_{+}(\boldsymbol{\rho}_1) = \frac{-ik}{z_1} e^{i2\pi k z_1} e^{i\pi k {\boldsymbol{\rho}_1}^2 \left(\frac{1}{z_1} - \frac{1}{f}\right)} \int_{-\infty}^{\infty} E(\boldsymbol{\rho}_0) P(\boldsymbol{\rho}_1) e^{\frac{-i2\pi k \boldsymbol{\rho}_1 \boldsymbol{\rho}_0}{z_1}} e^{\frac{i\pi k {\boldsymbol{\rho}_0}^2}{z_1}} d^2\boldsymbol{\rho}_0 \tag{2.25}$$

Using an additional Rayleigh-Sommerfeld diffraction integral under the Fresnel approximation, we propagate the field $E_{+}(\boldsymbol{\rho}_1)$ emerging from the lens to the image plane $\boldsymbol{\rho}_2$:

$$E(\boldsymbol{\rho}_2) = \frac{-ik}{z_2} e^{i2\pi k z_2} \int_{-\infty}^{\infty} E_{+}(\boldsymbol{\rho}_1) e^{\frac{i\pi k}{z_2}(\boldsymbol{\rho}_2 - \boldsymbol{\rho}_1)^2} d^2\boldsymbol{\rho}_1 \tag{2.26}$$

Inputting (2.25), combining the terms with ${\boldsymbol{\rho}_1}^2$ in the exponent and taking the ${\boldsymbol{\rho}_2}^2$ term, which is independent of the integration variables, outside the integral, we obtain:

$$E(\boldsymbol{\rho}_2) = \frac{-k^2}{z_2 z_1} e^{i2\pi k(z_2 + z_1)} e^{\frac{i\pi k}{z_2}{\boldsymbol{\rho}_2}^2} \int_{-\infty}^{\infty}\int_{-\infty}^{\infty} E(\boldsymbol{\rho}_0) P(\boldsymbol{\rho}_1) e^{i\pi k {\boldsymbol{\rho}_1}^2 \left(\frac{1}{z_2} + \frac{1}{z_1} - \frac{1}{f}\right)} e^{-i2\pi k \boldsymbol{\rho}_1 \left(\frac{\boldsymbol{\rho}_0}{z_1} + \frac{\boldsymbol{\rho}_2}{z_2}\right)} e^{\frac{i\pi k {\boldsymbol{\rho}_0}^2}{z_1}} d^2\boldsymbol{\rho}_1 d^2\boldsymbol{\rho}_0 \tag{2.27}$$

For the in-focus case, the lens-makers law $\frac{1}{z_1} + \frac{1}{z_2} = \frac{1}{f}$ applies, where f is the focal length of the lens, leading to the first squared-bracket exponential term in (2.27) becoming unity. We may introduce the magnification, $M = -\frac{z_2}{z_1}$, allowing (2.27) to be recast as:

$$E(\boldsymbol{\rho}_2) = \frac{-k^2}{{z_1}^2 M} e^{i2\pi k z_1 (1 - M)} e^{\frac{i\pi k {\boldsymbol{\rho}_2}^2}{z_2}} \int_{-\infty}^{\infty}\int_{-\infty}^{\infty} E(\boldsymbol{\rho}_0) P(\boldsymbol{\rho}_1)\, e^{\frac{-i2\pi k \boldsymbol{\rho}_1}{z_1}\left(\boldsymbol{\rho}_0 - \frac{\boldsymbol{\rho}_2}{M}\right)} e^{\frac{i\pi k {\boldsymbol{\rho}_0}^2}{z_1}} d^2\boldsymbol{\rho}_1 d^2\boldsymbol{\rho}_0 \tag{2.28}$$

We now introduce what is known as the coherent spread function (CSF) [23], defined by:

$$CSF\left(\frac{k\boldsymbol{\rho}_0}{z_1}\right) = \frac{k^2}{{z_1}^2 M} \int_{-\infty}^{\infty} P(\boldsymbol{\rho}_1) e^{-\frac{i2\pi k \boldsymbol{\rho}_1 \cdot \boldsymbol{\rho}_0}{z_1}} d^2\boldsymbol{\rho}_1 \tag{2.29}$$

Comparing the (2.30) with the Fourier transform $\mathcal{P}$ of the pupil function P, the CSF is simply a scaled version of the Fourier transform of P:

$$\mathcal{P}\left(\frac{k\boldsymbol{\rho}_0}{z_1}\right) = \int_{-\infty}^{\infty} P(\boldsymbol{\rho}_1) e^{-\frac{i2\pi k \boldsymbol{\rho}_1 \cdot \boldsymbol{\rho}_0}{z_1}} d^2\boldsymbol{\rho}_1 \tag{2.30}$$

The CSF is also known as the impulse response and Green's function [23]:

$$CSF\left(\frac{k\boldsymbol{\rho}_0}{z_1}\right) = \frac{k^2}{{z_1}^2 M} FT\{P(\boldsymbol{\rho}_1)\} \tag{2.31}$$

Substituting (2.30) into (2.29) we obtain the important result:

$$E(\boldsymbol{\rho}_2) = -e^{i2\pi k z_1(1-M)} e^{\frac{i\pi k \boldsymbol{\rho}_2{}^2}{z_2}} \int_{-\infty}^{\infty} E(\boldsymbol{\rho}_0) CSF\left(\boldsymbol{\rho}_0 - \frac{\boldsymbol{\rho}_2}{M}\right) e^{\frac{i\pi k \boldsymbol{\rho}_0{}^2}{z_1}} d^2\boldsymbol{\rho}_0 \tag{2.32}$$

It may be shown [19] that the quadratic phase factor inside the integral in (2.33) can be approximated by unity. The image and object fields $E(\boldsymbol{\rho}_0)$ and $E(\boldsymbol{\rho}_2)$ are now manifestly related by a convolution:

$$E(\boldsymbol{\rho}_2) = -e^{i2\pi k z_1(1-M)} e^{\frac{i\pi k \boldsymbol{\rho}_2{}^2}{z_2}} \int_{-\infty}^{\infty} E(\boldsymbol{\rho}_0) CSF\left(\boldsymbol{\rho}_0 - \frac{\boldsymbol{\rho}_2}{M}\right) d^2\boldsymbol{\rho}_0 \tag{2.33}$$

That is, the function $CSF(\boldsymbol{\rho})$ acts as an imaging propagator:

$$E(\boldsymbol{\rho}_2) = -e^{i2\pi k z_1(1-M)} e^{\frac{i\pi k \boldsymbol{\rho}_2{}^2}{z_2}} [E_0 \otimes CSF]_{\boldsymbol{\rho}_2} \tag{2.34}$$

The pre-factor term $e^{2\pi i z_1(1-M)/\lambda}$ corresponds to a fixed, uniform phase, and may generally be discarded, since it plays no role in imaging. In addition, we are only interested in the detected intensity at the image plane for imaging applications, resulting in the quadratic phase factor $e^{i\pi k \boldsymbol{\rho}_2{}^2/z_2}$ also playing no role in imaging. Hence, it is also discarded. We therefore arrive with the final image field:

$$E(\boldsymbol{\rho}_2) = \int_{-\infty}^{\infty} E(\boldsymbol{\rho}_0) CSF\left(\boldsymbol{\rho}_0 - \frac{\boldsymbol{\rho}_2}{M}\right) d^2\boldsymbol{\rho}_0 \tag{2.35}$$

From the Fourier transform of the CSF we define a radiant-field imaging propagator:

$$CTF(\boldsymbol{q}_1) = \int_{-\infty}^{\infty} CSF(\boldsymbol{\rho}_0) e^{\frac{-i2\pi k \boldsymbol{\rho}_0 \cdot \boldsymbol{\rho}_1}{z_1}} d^2\boldsymbol{\rho}_0 = FT\{CSF(\boldsymbol{\rho}_0)\} \tag{2.36}$$

This is referred to as the coherent transfer function (CTF), which is simply a scaled version of the pupil function where, from the form of the Fourier kernel, one can see that the spatial frequency variable of the returned transform is $\boldsymbol{q}_1 = k\boldsymbol{\rho}_1/z_1$ [23]:

$$CTF(\boldsymbol{\rho}_1) = \frac{k^2}{z_1{}^2 M} P(\boldsymbol{\rho}_1) \tag{2.37}$$

The convolution relation given in (2.35) translates in the frequency domain to a simple product relation, given by [23]:

$$\mathcal{E}'(\boldsymbol{q}_1) = CTF(\boldsymbol{q}_1)\mathcal{E}(\boldsymbol{q}_1) \tag{2.38}$$

where (2.12) is used to define $\mathcal{E}(\boldsymbol{q})$ and $\mathcal{E}'$ defines the transform of $E(\boldsymbol{\rho}_2)$.

Equation (2.38) shows that the range of values of $\boldsymbol{q}_1$ for which image formation will be transferred are limited by the pupil function P (as $CTF \propto P$). It is noteworthy that a plane-wave Fourier component emitted by the object is propagated unaltered from the object plane to the lens plane. With the above derived relations we have established the foundation of the Fourier optics theory of imaging with lenses. The CSF and CTF functions apply specifically to the case of imaging with coherent fields. We may move to discuss the more relaxed case of imaging with incoherent fields, requiring the introduction of additional field propagator functions.

2.3 Incoherent Field Propagation

Our discussion so far has been limited to the case of coherent illumination fields, with the time dependence of the fields assumed to be perfectly harmonic, an assumption that is not generally valid. For the case of the local phase being continuously random, the resulting image field phase and amplitude are generally random, since a superposition of object fields forms the image field. In this case, the light fields must be dealt with statistically rather than deterministically [24]. Such statistical averages are taken over periods much longer than the coherence time of the illuminating field, where the coherence time is defined as [25]:

$$\tau \approx \frac{\lambda^2}{c\Delta\lambda} \tag{2.39}$$

where λ is the central wavelength of the source, $\Delta\lambda$ is the spectral bandwidth of the source and c is the universal wave constant. Defining a time average by $\langle \dots \rangle$, the intensity of a light field is then [26]:

$$I(\boldsymbol{\rho}) = \langle |E(\boldsymbol{\rho}, t)|^2 \rangle \tag{2.40}$$

Here, E is taken to be explicitly time dependent, and we henceforth write $E(\boldsymbol{\rho}, t)$ as $E(\boldsymbol{\rho})$ for simplicity. In a similar manner to the coherent field spectrum, we introduce the intensity spectrum, definted as the Fourier transform of the intensity [23]:

$$\mathfrak{T}(\boldsymbol{q}) = \int_{-\infty}^{\infty} I(\boldsymbol{\rho})\, e^{-i2\pi \boldsymbol{q}\cdot\boldsymbol{\rho}} d^2\boldsymbol{\rho} \tag{2.41}$$

2.4 Incoherent Imaging with a lens

In a similar vein to the coherent imaging functions used to define coherent imaging via a focusing lens, we may introduce a pair of similar functions to facilitate the incoherent imaging of an intensity distribution or spectrum via a focusing lens. The point-spread function (PSF) and optical transfer function (OTF) play similar roles to the CSF and CTF for incoherent imaging, being defined using the CSF and CTF respectively [23]:

$$PSF(\boldsymbol{\rho}) = \frac{1}{k^2\Omega_0} |CSF(\boldsymbol{\rho})|^2 \tag{2.42}$$

and:

$$OTF(\boldsymbol{q}) = \frac{1}{k^2\Omega_0} \int_{-\infty}^{\infty} CTF\left(\boldsymbol{q} + \frac{1}{2}\boldsymbol{q}'\right) CTF^*\left(\boldsymbol{q} - \frac{1}{2}\boldsymbol{q}'\right) d^2\boldsymbol{q}' \tag{2.43}$$

Equation (2.42) states that the PSF is equal to a normalized squared modulus of the CSF, and equation (2.43) states that the OTF is equal to a normalized autocorrelation of the CTF where; when referenced to the object plane, the pupil solid angle is [23]:

$$\Omega_0 = \frac{1}{{z_1}^2} \int_{-\infty}^{\infty} |P(\boldsymbol{\zeta})|^2 d^2\boldsymbol{\zeta} \tag{2.44}$$

where $\boldsymbol{\zeta}$ is some arbitrary variable. Hence, with use of (2.42) and (2.43), we obtain the fundamental equations for incoherent imaging [23]:

$$I_2(\boldsymbol{\rho}_{2d}) = \frac{\Omega_0}{M^2} \int_{-\infty}^{\infty} PSF(\boldsymbol{\rho}_2 - \boldsymbol{\rho}_0) I_0(\boldsymbol{\rho}_0) d^2\boldsymbol{\rho}_0 \tag{2.45}$$

and:

$$\mathfrak{T}_2(\boldsymbol{q}) = \Omega_0 OTF(\boldsymbol{q}) \mathfrak{T}_0(\boldsymbol{q}) \tag{2.46}$$

Analogous to the CSF characterisation of imaging with a coherent field, the PSF characterises imaging with an incoherent intensity. Similarly, the OTF characterisation of imaging with an incoherent intensity spectrum is analogous to how the CTF characterises imaging with a coherent radiant field. Having established the necessary theory describing the cases of coherent and incoherent illumination for a focused image, we may move to demonstrating this computationally.

3. Fundamental Computational Simulation

3.1 Focused coherent and incoherent illumination

Having provided a comprehensive overview of the theoretical foundations of Fourier optics and introduced the key tools required to model an optical system of choice, we will now move to simulate computationally such a model. Firstly, we will model a simple optical configuration consisting of a source projection onto a focal plane via a lens. Following from this, we will move to a more elaborate setup, which will be representative of the currently operational TWIN-MIC TXM/STXM machine. Once such a complex model is established, alterations will be made in order to image in a SIM mode with the model, providing information on the capabilities of such an X-ray device to image in a SIM mode.

To begin with, we will model a simple optical configuration consisting of a focused source illumination in the de-magnified case, as depicted in figure 3.1. For this, the illumination is provided by a monochromatic source field E illuminating an amplitude transmission object with transmission function t, located at the source plane $\boldsymbol{\rho}_0$. The illumination source is thus a product of the source field and transmission object, $E(\boldsymbol{\rho}_0)t(\boldsymbol{\rho}_0)$. We choose our transmission object to be a sinusoidal grating of period α and some total number of periods K, with the grating modulated within the $\hat{\boldsymbol{e}}_x$ direction. The reasons of choice of such an object will become clearer in later chapters.

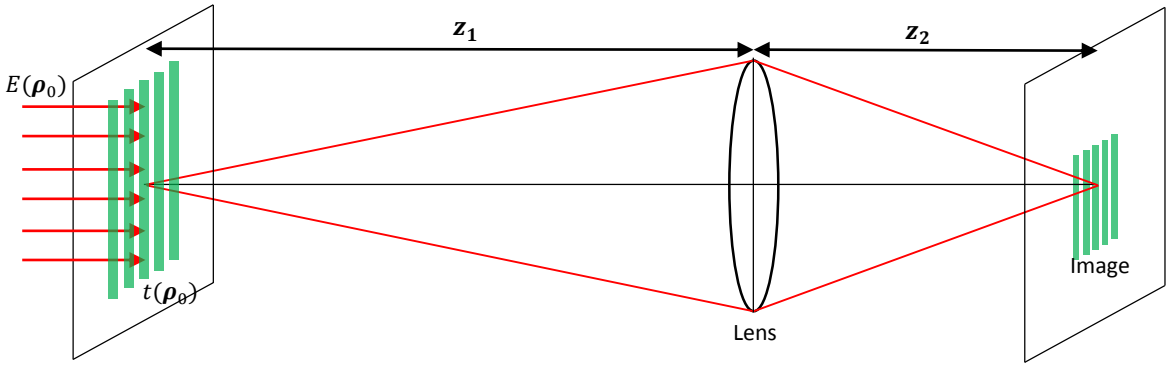

Figure 3.1: Diagram of simple optical system for fringe projection onto a focused plane

As we can see in figure 3.1, the required objects that need be constructed in order to generate the focused image are the source illumination and lens profile. This may be better visualised with use of the theory developed in chapter 2, whereby the coherent focused image of an illumination source $E(\boldsymbol{\rho}_0)t(\boldsymbol{\rho}_0)$ via a lens with pupil function P is given by:

$$E_2(\boldsymbol{\rho}_2) = FT^{-1}\left(CTF(\boldsymbol{q})FT\big(E_0(\boldsymbol{\rho}_0)t(\boldsymbol{\rho}_0)\big)\right) \tag{3.1}$$

and where $CTF \propto P$. The remarkable benefits in terms of simplicity when developing a model using Fourier optics as opposed to geometrical optics is clearly demonstrated here. In the same vain, we may also obtain the incoherent image intensity present at the focused image plane using the developments of chapter 2:

$$I_2(\boldsymbol{\rho}_2) = FT^{-1}\left(OTF(\boldsymbol{q})FT\big(I_0(\boldsymbol{\rho}_0)t(\boldsymbol{\rho}_0)\big)\right) \tag{3.2}$$

The reasons of comparison between the cases of coherent and incoherent illumination will become clearer in due course. Using (3.1), we may move to simulating the system depicted in figure 3.1. As mentioned in chapter 1, simulations for this project were carried out in the Mathworks Matlab NDE. As such, for simulation purposes, the grating object, and indeed all other simulated objects, may be represented by a finite number of samples N.

For the grating object, we choose these to be in both $\hat{\boldsymbol{e}}_x$ and $\hat{\boldsymbol{e}}_y$ directions, with corresponding equivalent sampling intervals Δ, giving a total span in a single dimension of $N\Delta$. The grating is defined by a period $\alpha = 940nm$ and total periods $K = 15$, corresponding to a total width $14.1\mu m$. We represent the grating by $N = 512$ samples, and consequently by $\Delta = 27.5nm$ sampling intervals,

yielding adequate sampling of each grating period. The source field is chosen to have amplitude unity, for purposes of simplicity. The resulting source illumination, the product of the source field and grating object $E(\boldsymbol{\rho}_0)t(\boldsymbol{\rho}_0)$, is shown in figures 3.2a and 3.2b, corresponding to the illumination field and illumination intensity respectively.

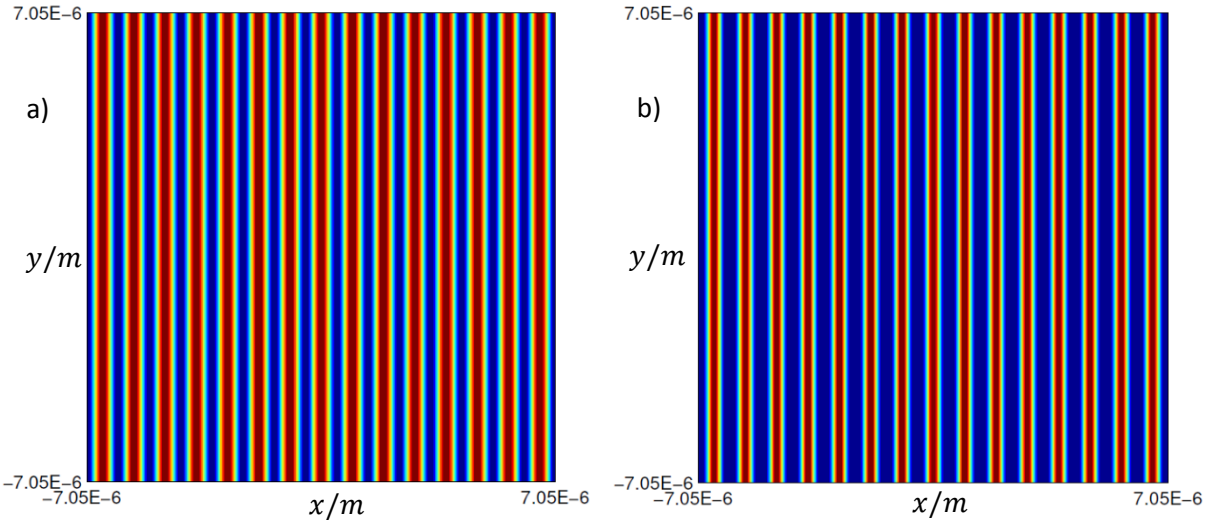

Figure 3.2: a) Source field **b)** Source intensity

Following from (3.1) and (3.2), Fourier transforms of the source field and source intensity must be taken, the product of these transforms taken with the respective CTF and OTF of the system and finally the inverse Fourier transform taken, in order to obtain the final field/intensity image. We thus require a Fourier transform to be taken of the objects displayed in figures 3.3a and 3.3b. With such objects represented discretely, so too will the Fourier transforms involved in the simulation be represented by discrete summations as opposed to integrations over a continuous variable. Such a transform is referred to as a discrete Fourier transform [27]:

$$\mathcal{F}(p\Delta\boldsymbol{q}) = \sum_{m=0}^{N_{\boldsymbol{\rho}}-1} F(m\Delta\boldsymbol{\rho}) e^{-i2\pi\left(\frac{pm}{N_{\boldsymbol{\rho}}}\right)} \tag{3.3}$$

where $\Delta\boldsymbol{q}$ is the co-ordinate spacing of the retuned set of frequencies, $\Delta\boldsymbol{\rho}$ is the co-ordinate spacing of the set of initial field positions, $N_{\boldsymbol{\rho}}$ is the number of initial field positions and m and p are integers. Such a transform is most rapidly computed using the fast Fourier transform, which, for a total of $N_{\boldsymbol{\rho}}$ points requires order $N_{\boldsymbol{\rho}} log N_{\boldsymbol{\rho}}$ complex multiplications and additions; the computation is fastest if the number of samples $N_{\boldsymbol{\rho}}$ is chosen to be a power of 2 [27]. Although highly efficient, Matlab's fast Fourier transform routine is problematic in that it relies on the principles of periodic convolution [28], meaning that it treats the object being transformed as periodic, which reflects in the resulting transform. As such, it is necessary to sufficiently zero-pad the object prior to transforming, such that the period of the zero-padded object is at least twice the period of the unpadded object, in order to yield a transform free from artefacts resulting from periodic convolution [28]. As such, we zero-pad the object field and intensity arrays to twice their original size, moving from $N = 512$ for each dimension to $N = 1024$. The zero-padded field and intensity are plotted in figures 3.3a and 3.3b. As a final alteration to the source field, we seek to rotate it by some arbitrary angle such that, should any diffraction effects or related artefacts arise due to the object itself, which will likely be present in some parallel fashion to the grating dimensions, we will be able to conclude these have arisen due to the object itself and not due to insufficient zero-padding. Such insufficient zero-padding would lead to artefacts parallel to the complete array edges, which may be distinguished from the object edges if the object is rotated by some arbitrary angle. Henceforth, we choose an angle 10°, leading to array dimension sizes $N = 1189$; the rotated source field and intensity plotted in figures 3.4a and 3.4b.

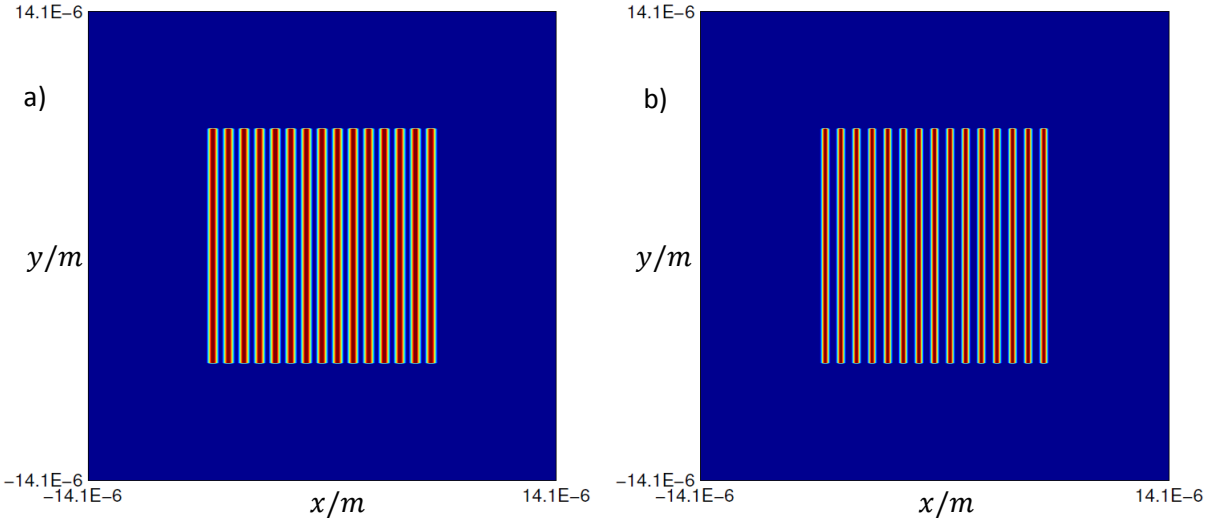

Figure 3.3: a) Zero-padded source field **b)** Zero-padded source intensity

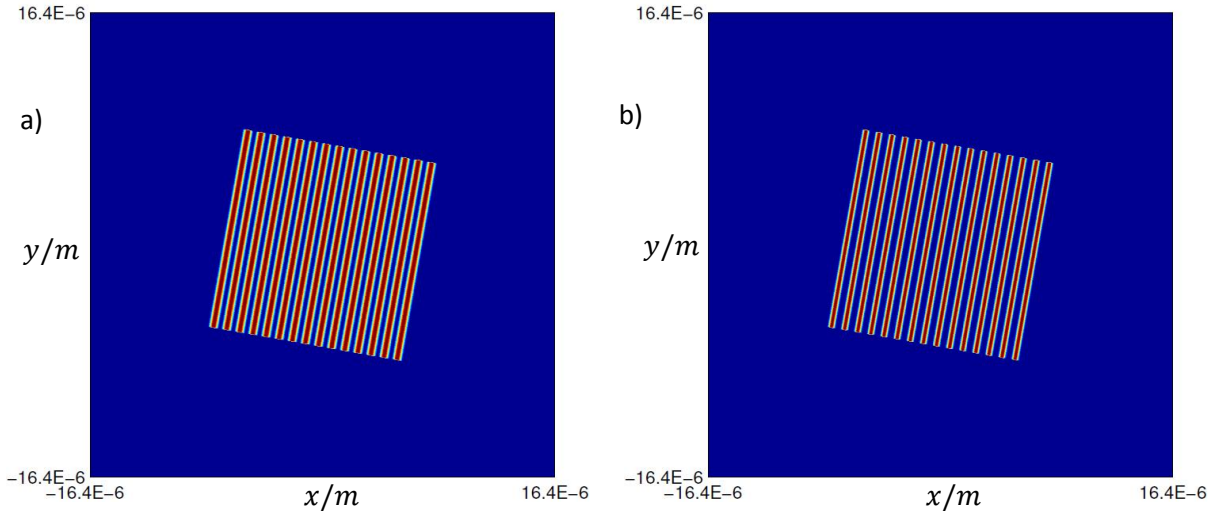

Figure 3.4: a) Rotated and zero-padded source field **b)** Rotated and zero-padded source intensity

It is a property of almost all fast Fourier transform algorithms, including Matlab's own fast Fourier transform function, that when the input function to the transform is given as a set of positions, $\{\boldsymbol{\rho}\}$, having N values of position with spacing Δ, the output function is returned as a set $\{\boldsymbol{q}\}$ of frequencies having N values of frequency with spacing $1/(N\Delta)$ [27]. For an object represented by a set of N positions with spacing Δ, we may determine the spacing for the conjugate plane positions in the system of study and also the spacing for the conjugate plane frequency values, as illustrated in figure 3.5.

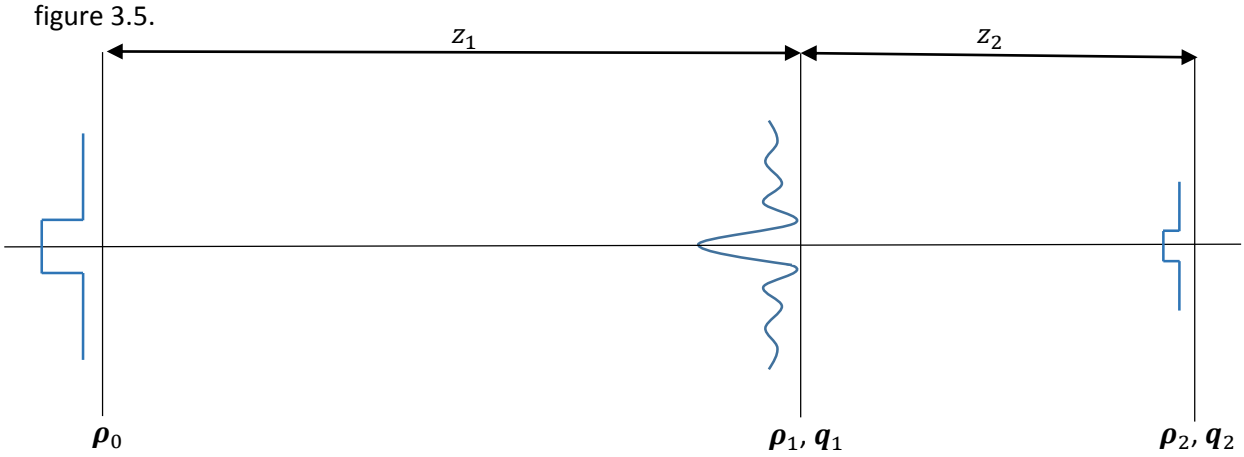

Figure 3.5: Diagram of optical system co-ordinate planes

As already stated from the form of the Fourier kernel, one can see that the spatial frequency variable of the returned transform (i.e. the frequency conjugate to $\boldsymbol{\rho}_0$) is $\boldsymbol{q}_1 = \boldsymbol{\rho}_1 k/z_1$. We thus find that the various conjugate co-ordinate position and spatial frequency spacings involved in the system are related through the following co-ordinate transforms:

$$\Delta_{\boldsymbol{q}_1} = \frac{1}{N\Delta_{\boldsymbol{\rho}_0}} \tag{3.4}$$

$$\Delta_{\boldsymbol{\rho}_1} = \frac{z_1\Delta_{\boldsymbol{q}_1}}{k} = \frac{z_1}{kN\Delta_{\boldsymbol{\rho}_0}} \tag{3.5}$$

$$\Delta_{\boldsymbol{q}_2} = \frac{-1}{N\Delta_{\boldsymbol{\rho}_1}} = -\frac{k\Delta_{\boldsymbol{\rho}_0}}{z_1} \tag{3.6}$$

$$\Delta_{\boldsymbol{\rho}_2} = \frac{z_2\Delta_{\boldsymbol{q}_2}}{k} = \frac{-z_2\Delta_{\boldsymbol{\rho}_0}}{z_1} = M\Delta_{\boldsymbol{\rho}_0} \tag{3.7}$$

where N is the number of values of position with spacing Δ_i in the i[th] co-ordinate plane. We see that the conjugate co-ordinates for each plane are related by a constant relation involving the wave-number $k = n/\lambda$ and the propagation distance z_i, due to the form of the Fourier kernel. In addition, due to the inverse transform being present for transformation from plane 1 to plane 2, a negative sign enters the transform relations in (3.6). We see that the final plane is a linearly scaled version of the object plane, with the scaling factor represented by a constant M, the magnification, which has already been introduced as $M = -z_2/z_1$. Thus, for a system with $z_1 > z_2$, we obtain a de-magnified (smaller) image of the object as represented in figure 3.1, and conversely for a system with $z_1 < z_2$, we obtain a magnified (larger) image of the object.

For our simple model system we assign modelling parameters of illumination wavelength λ = 2.49nm, propagation distances z_1 = 52mm and z_2 = 6.75mm and lens focal length f = 6mm. These values are chosen as they correspond to the specific wavelength and length parameters of TWIN-MIC. We see that with such propagation distances, our system is imaging in a de-magnified setup with magnification $M \approx -0.129$.

We see that for an ideal lens of infinite diameter, the image achieved at the focal plane will be completely faithful to the source image, being a scaled image of identical characteristics. However, this is not a realistic model as the lens will certainly have some finite diameter, even if it is large in comparison to the system dimensions. We will see that such a restriction of the frequencies permitted leads to interesting artefacts in the focused image. For a simple imaging lens, we describe the pupil as a thin, transparent disc, with the pupil function P taking the form of a *circ* function [19]:

$$P(\boldsymbol{\rho}_1) = \begin{cases} 0 \text{ if } |\boldsymbol{\rho}_1| > D \\ 1 \text{ if } |\boldsymbol{\rho}_1| < D \end{cases} \tag{3.8}$$

Here, D is the diameter of the circular lens, where it is assumed that the lens axis also corresponds to the optical axis of the system, as shown in figure 3.1. We may choose $D = 500\mu m$, again a suitable lens diameter for soft X-ray microscopy, and a value that will be very appropriate in later chapters. Correspondingly, the normalized CTF and CSF may be defined as:

$$CTF(\boldsymbol{q}_1) = \begin{cases} 0 \text{ if } |\boldsymbol{q}_1| > kD/2z_1 \\ 1 \text{ if } |\boldsymbol{q}_1| < kD/2z_1 \end{cases} \tag{3.9}$$

$$CSF(\boldsymbol{\rho}_0) = \frac{\pi}{4}\left(\frac{kD}{2z_1}\right)^2 jinc\left(\frac{\pi\boldsymbol{\rho}_0 kD}{z_1}\right) \tag{3.10}$$

where the $jinc$ function is defined as [19]:

$$jinc(2\pi kx) = \frac{J_1(2\pi kx)}{\pi kx} \tag{3.11}$$

where J_1 is the cylindrical Bessel function of order 1 [17]. We see that, for ease of calculation, the constant prefactors for the CTF relation have been dropped. From (3.1) we see that we require only the CTF in order to obtain the focused field. In addition, from the form of the CTF in (3.5) it is clear that if the field distribution in the object plane contains a large spread of frequencies, then only the subset of these supported by the CTF are projected to the image plane. In this manner, the CTF described by (3.5) behaves as a low-pass filter, yielding a maximum spatial bandwidth $\Delta\boldsymbol{q}$ at the image plane, where $\Delta\boldsymbol{q}$ corresponds to the CTF wavevector span. This low-pass filter behaviour results in interesting phenomena in the image fields and intensities, as we will see in due course. Figure 3.6a and 3.6b give plots of the system CTF in real space co-ordinates.

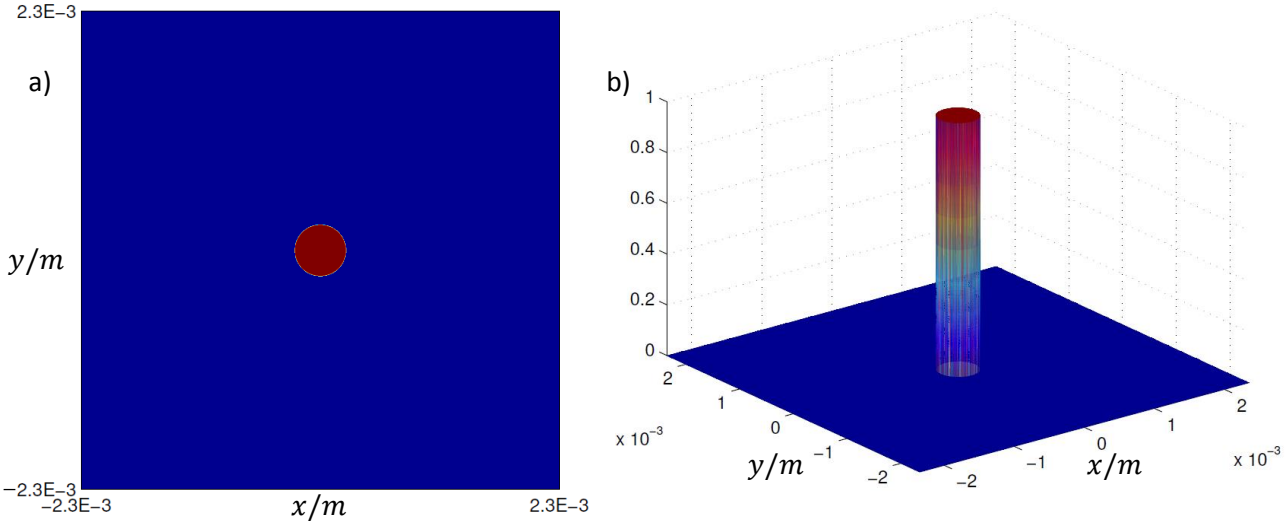

Figure 3.6: a) Contour plot of system CTF for circular lens $D = 500\mu m$ **b)** Surface plot of CTF

The CTF of course applies in the case of coherent field propagation. From (3.2) we see that we may also obtain the incoherent intensity image at the focused plane through application of the system OTF to the source intensity transform, acting in a similar vain to the CTF as a low frequency support. From (2.43) we appreciate that the OTF is obtained from the autocorrelation of the CTF, which may be carried out both computationally and analytically for the simple case of the *circ* pupil function [23]. The analytical OTF, and corresponding PSF, are:

$$OTF(\boldsymbol{q}_1) = \begin{cases} 0 \text{ if } |\boldsymbol{q}_1| > kD/2z_1 \\ \frac{2}{\pi}\left(cos^{-1}\left(\frac{z_1\boldsymbol{q}_1}{kD}\right) - \frac{z_1\boldsymbol{q}_1}{kD}\left(1 - \left(\frac{z_1\boldsymbol{q}_1}{kD}\right)^2\right)^{1/2}\right) \text{ if } |\boldsymbol{q}_1| < kD/2z_1 \end{cases} \tag{3.12}$$

$$PSF(\boldsymbol{\rho}_0) = \frac{\pi}{4}\left(\frac{kD}{2z_1}\right)^2 jinc^2\left(\frac{\pi\boldsymbol{\rho}_0 kD}{z_1}\right) \tag{3.13}$$

Figures 3.7a and 3.7b give plots of the system OTF in real space co-ordinates. Armed now with both the system CTF and OTF, alongside the source field and source intensity, we may readily go about calculation of the focused image field and intensity using (3.1) and (3.2). We see the result of such calculation in figures 3.8a and 3.8b.

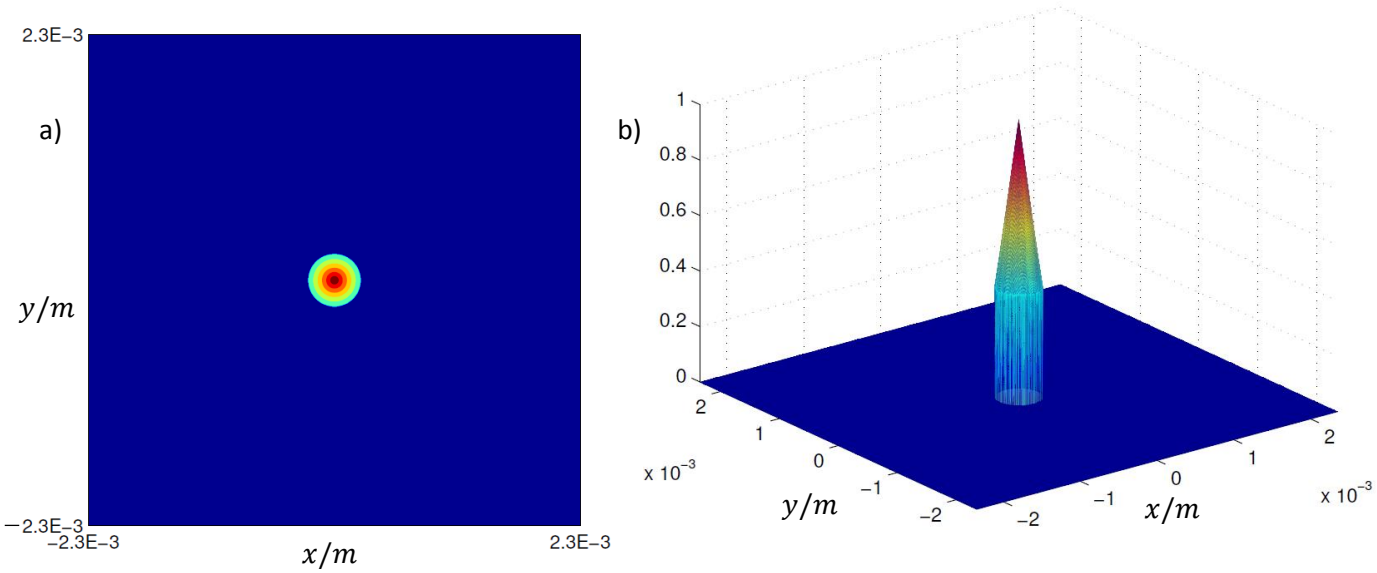

Figure 3.7: a) Contour plot of system OTF for circular lens $D = 500\mu m$ **b)** Surface plot of OTF

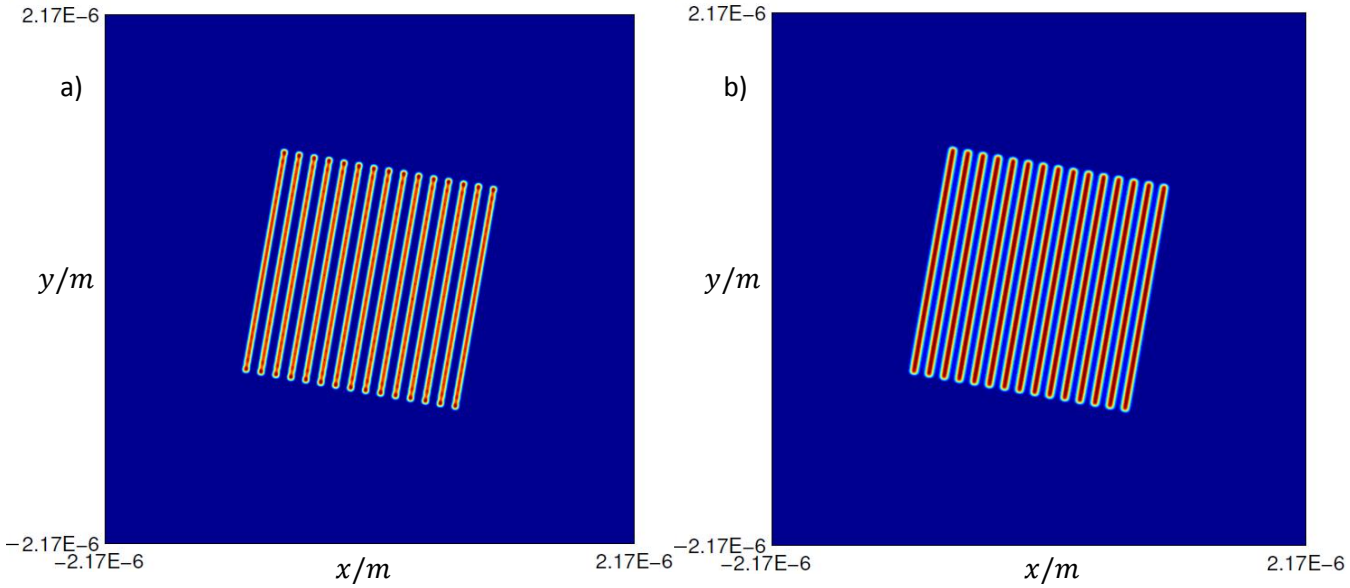

Figure 3.8: a) Focused coherent field **b)** Focused incoherent intensity

Looking at the final coherent field and incoherent intensity in figures 3.8a and 3.8b, we see that the final images in both cases correspond well with the source field and intensity plotted in figures 3.4a and 3.4b respectively, with some minor differences. The coherent field appears to have slightly thinner fringes, with both the coherent field and incoherent intensity having more rounded edges than the square source fringe edges. In addition, the coherent field amplitude appears to have some high frequency oscillation components present at fringe ends, visible as darker artefacts. This ringing artefact results from Gibbs phenomenon, the unusual fashion in which a piecewise continuously differentiable periodic function behaves at a discontinuous jump [29]: the nth partial sum of the Fourier series of the periodic function oscillates with large amplitudes near the jump, which causes an increase in the maximum of the partial sum above that of the function itself. This overshoot approaches a finite limit as opposed to decaying as the frequency increased. From the point of view of the system in question, the Gibbs phenomenon is the step response of the low-pass filter, or circular pupil, present in the system, with the oscillations referred to as ringing artefacts. This is the interesting affect alluded to earlier as a result of only a subset of the object frequency distribution being supported by the system CTF. In comparison, we see that the case of incoherent illumination provides a much more uniform intensity variation in comparison to the coherent illumination case.

3.2 3D Imaging through Defocus

We have so far only operated within a 2D formalism in that only scalar fields in transverse planes have been considered; such fields having been propagated between focused planes. We will now relax the in-focus imaging restriction in order to image with propagation distances not obeying the lens maker's equation, allowing the image and object planes to be out of focus with respect to one another. This may be achieved through a combination of in-focus imaging followed by an additional defocus operation. We are fortunate in that the functions describing these operations have already been introduced in chapter 1, with the in-focus imaging functions given by the CTF for coherent fields and the OTF for incoherent intensities. The defocus represents a free-space propagation between the focused plane to an out-of-focus plane, and as such the functions describing this free-space propagation have already been presented as Fresnel free-space propagators H (2.20) or $\mathcal{H}$ (2.21). Hence, we will consolidate both the in-focus imaging and defocus propagation operations under a 3D imaging framework, with our calculations remaining within the domain of the Fresnel approximation.

3.2.1 Defocused Fields

The free-space field propagation from a plane at $z = 0$ to a plane at $z > 0$ was described in chapter 1 as a convolution operation:

$$E(\boldsymbol{\rho}, z) = |H(\boldsymbol{\rho}, z) \otimes E(\boldsymbol{\rho}, 0)|_{\boldsymbol{\rho}} \tag{3.14}$$

where H is the Fresnel free-space propagator (2.20). The associated free-space radiant field propagation is then described by:

$$\mathcal{E}(\boldsymbol{q}; z) = \mathcal{H}(\boldsymbol{q}; z)\mathcal{E}(\boldsymbol{q}; 0) \tag{3.15}$$

where $\mathcal{H}$ is the corresponding transfer function in Fourier space (2.21). We see that $E(\boldsymbol{q}, z)$ may be calculated either directly from (3.14) or indirectly from an inverse Fourier transform of (3.15):

$$E(\boldsymbol{\rho}, z) = FT^{-1}\{\mathcal{H}(\boldsymbol{q}; z)\mathcal{E}(\boldsymbol{q}; 0)\} \tag{3.16}$$

For simplification purposes, we define $z = 0$ as the in-focus plane position and $z \neq 0$ as the out-of-focus plane position. As the Helmholtz equation supports propagation in both the positive and negative plane directions, the defocus z may be either positive or negative. An advantage of the use of (3.16) over the Fresnel diffraction integral is that there is no $1/z$ factor present as a pre-factor to the integral or within the exponent itself, causing (3.16) to be well suited for defocus values of z that approach 0, or are particularly small. We note, however, that the scaling of the exponent with z in the exponent for large defocus values can result in aliasing of the field, a phenomena that will be described in further detail in due course. We thus conclude that the usual Fresnel diffraction integral is better suited for large values of defocus [23].

From the form of (3.14) we can see that such a defocus operation may be combined in situ with imaging through a lens. We may therefore introduce a generalised, arbitrary focus imaging operator from the combination of in-focus imaging with defocus which is applicable to both coherent and incoherent fields.

For coherent illumination, the radiant field for the case of a focused object plane and defocused image plane is:

$$\mathcal{E}_1(\boldsymbol{q}; z) = \mathcal{H}(\boldsymbol{q}; z)CTF(\boldsymbol{q})\mathcal{E}_0(\boldsymbol{q}; 0) \tag{3.17}$$

where $CTF(\boldsymbol{q})$ is responsible for the in-focus imaging and $\mathcal{H}(\boldsymbol{q}; z)$ is responsible for the de-focus imaging. We then obtain the image field through an inverse Fourier transform of (3.17), in parallel to the focused imaging operation (3.15). We may define a 3D CTF using the convention that $z > 0$ corresponds to the image or object plane moving away from the imaging lens:

$$CTF(\boldsymbol{q};z) = CTF(\boldsymbol{q})\mathcal{H}(\boldsymbol{q};z) \tag{3.18}$$

Using (2.21), this becomes:

$$CTF(\boldsymbol{q};z) = CTF(\boldsymbol{q})e^{i2\pi kz}e^{-\frac{i\pi z}{k}\boldsymbol{q}^2} \tag{3.19}$$

Here, we have arrived at a mixed representation of the CTF, as it is a function of both spatial and frequency co-ordinates. Analogous to the in-focus CTF being defined by the imaging device pupil (2.37), the CTF defined by (3.19) can be thought of as being defined by a generalized 3D pupil [23].

Parallel to the in-focus CSF definition, the 3D CTF Fourier transform allows us to obtain a 3D CSF:

$$CSF(\boldsymbol{\rho},z) = FT\{CTF(\boldsymbol{q};z)\} \tag{3.20}$$

From (3.20), we obtain:

$$CSF(\boldsymbol{\rho},z) = e^{i2\pi kz}\int_{-\infty}^{\infty} CTF(\boldsymbol{q})\, e^{i2\pi \boldsymbol{q}\cdot\boldsymbol{\rho}-\frac{i\pi z}{k}\boldsymbol{q}^2} d^2\boldsymbol{q} \tag{3.21}$$

From (3.14) we see that the object and image fields are related by the convolution integral:

$$E_2(\boldsymbol{\rho}_2,z_1) = \int_{-\infty}^{\infty} CSF(\boldsymbol{\rho}_2-\boldsymbol{\rho}_0,z_1-z_0)E_0(\boldsymbol{\rho}_0,z_0)d^2\boldsymbol{\rho}_0 \tag{3.22}$$

where z_0 and z_1 correspond to the object and image defocus, respectively. In addition, we see that no integration over z_0 is performed, indicating that $E_2(\boldsymbol{\rho}_2,z_1)$ remains implicitly a function of z_0. We are hence still dealing with 2D imaging from one plane to another between arbitrarily located planes.

3.2.2 Defocused Intensities

With the 3D imaging of coherent fields established with use of the 3D CSF and 3D CTF, we may investigate the case of 3D imaging with incoherent intensities. Only the intensities in the object and image planes will be of interest, as previously outlined, and as such we examined operational functions for intensity imaging. From (2.42), we have:

$$PSF(\boldsymbol{\rho},z) = \frac{1}{k^2\Omega}|CSF(\boldsymbol{\rho},z)|^2 \tag{3.23}$$

which, from (3.21), leads to:

$$PSF(\boldsymbol{\rho},z) = \frac{1}{k^2\Omega}\int_{-\infty}^{\infty}\int_{-\infty}^{\infty} CTF(\boldsymbol{q})CTF^*(\boldsymbol{q}')e^{i2\pi(\boldsymbol{q}-\boldsymbol{q}')\cdot\boldsymbol{\rho}}e^{-\frac{i\pi z}{k}(\boldsymbol{q}^2-\boldsymbol{q}'^2)}d^2\boldsymbol{q}d^2\boldsymbol{q}' \tag{3.24}$$

where the parameter Ω again denotes the solid angle of the aperture pupil (2.44). Introducing co-ordinate transformations [23]:

$$\boldsymbol{q}_c = \frac{1}{2}(\boldsymbol{q}+\boldsymbol{q}') \tag{3.25}$$

$$\boldsymbol{q}_d = \boldsymbol{q}-\boldsymbol{q}' \tag{3.26}$$

with related identities:

$$d^2\boldsymbol{q}d^2\boldsymbol{q}' = d^2\boldsymbol{q}_c d^2\boldsymbol{q}_d \tag{3.27}$$

$$\boldsymbol{q}^2-\boldsymbol{q}'^2 = 2\boldsymbol{q}_c\cdot\boldsymbol{q}_d \tag{3.28}$$

we arrive at [23]:

$$PSF(\boldsymbol{\rho},z) = \frac{1}{k^2\Omega}\int_{-\infty}^{\infty}\int_{-\infty}^{\infty} CTF\left(\boldsymbol{q}_c+\frac{1}{2}\boldsymbol{q}_d\right)CTF^*\left(\boldsymbol{q}_c-\frac{1}{2}\boldsymbol{q}_d\right)e^{i2\pi\boldsymbol{q}_d\cdot\boldsymbol{\rho}}e^{-\frac{i2\pi z}{k}\boldsymbol{q}_c\cdot\boldsymbol{q}_d}d^2\boldsymbol{q}_c d^2\boldsymbol{q}_d \tag{3.29}$$

corresponding to a 3D PSF. We thus describe incoherent intensity imaging in three dimensions by:

$$I_2(\boldsymbol{\rho}_2, z_1) = \Omega \int_{-\infty}^{\infty} PSF(\boldsymbol{\rho}_2 - \boldsymbol{\rho}_0, z_1 - z_0) I_0(\boldsymbol{\rho}_0, z_0) d^2\boldsymbol{\rho}_0 \tag{3.30}$$

In addition, we note that $I_2(\boldsymbol{\rho}_2, z_1)$ is implicitly a function of z_0 as (3.29) contains no integral over z_0. We again see that the 3D imaging operation is a disguised 2D imaging operation. With use of the 3D PSF we may obtain the 3D OTF using their implicit transform relation:

$$OTF(\boldsymbol{q}; z) = \int_{-\infty}^{\infty} PSF(\boldsymbol{\rho}, z) e^{-i2\pi \boldsymbol{q}\cdot\boldsymbol{\rho}} d^2\boldsymbol{\rho} \tag{3.31}$$

which, from (3.29), leads to:

$$OTF(\boldsymbol{q}; z) = \frac{1}{k^2\Omega} \int_{-\infty}^{\infty} CTF\left(\boldsymbol{q}_c + \frac{1}{2}\boldsymbol{q}_d\right) CTF^*\left(\boldsymbol{q}_c - \frac{1}{2}\boldsymbol{q}_d\right) e^{-\frac{i2\pi z}{k}\boldsymbol{q}_c\cdot\boldsymbol{q}} d^2\boldsymbol{q}_c \tag{3.32}$$

Equation (3.32) is entirely equivalent to:

$$OTF(\boldsymbol{q}; z) = \frac{1}{k^2\Omega} \int_{-\infty}^{\infty} CTF\left(\boldsymbol{q}_c + \frac{1}{2}\boldsymbol{q}_d; z\right) CTF^*\left(\boldsymbol{q}_c - \frac{1}{2}\boldsymbol{q}_d; z\right) d^2\boldsymbol{q}_c \tag{3.33}$$

where (3.19), the Fresnel definition of the 3D CTF, has been used. Thus, we see that the operations for in-focus imaging are entirely analogous to those for out-of-focus imaging, with $OTF(\boldsymbol{q}; z)$ equalling a normalized autocorrelation of $CTF(\boldsymbol{q}; z)$.

It is noted that for a spatial frequency q of zero, $OTF(0; z)$ is a constant, independent of the defocus z, identically equal to 1. This arises due to the normalization condition $\int_{-\infty}^{\infty} PSF(\boldsymbol{\rho}, z) dx = 1$, which stems from the principle of conservation of power which states that, in free space, light incurs no loss in power as it propagates between axial planes [29]. This fundamental principle was described in the opening introduction, and serves as the foundations of out-of-focus background rejection for SIM imaging.

3.2.3 Simulating defocus in the coherent and incoherent case

We may utilise the focused coherent field and incoherent intensity results displayed in figures 3.8a and 3.8b in order to simulate the field and intensity defocus under the theoretical architecture outlined so far.

Choosing to work in the frequency domain for each case, we may use both (3.19) and (3.33) for such propagations following lens imaging. As previously described, the Fourier transforms are implemented efficiently with use of the FFT algorithm [27]. However, care must be taken when evaluating the propagator term in each computation in order to avoid aliasing of the signal. Aliasing refers to an effect that causes different signals to become indistinguishable, or aliases of one another, when sampled. This follows from the Shannon Sampling Theorem [27], which details conditions for sufficiently fine sampling of the propagators. The smallest period p of the propagator occurs at the maximum value q_m of $q = |\boldsymbol{q}|$ and can be determined as follows [27]:

$$\frac{\pi z}{k} {q_m}^2 - \frac{\pi z}{k}(q_m - p)^2 = 2\pi \;\rightarrow p \cong \frac{k}{q_m z} \tag{3.34}$$

As already outlined, it is a property of almost all FFT algorithms that when the input function to the transform is given at a set of positions, $\{\boldsymbol{\rho}\}$, having N values of position with spacing Δ, the output function is returned at a set $\{\boldsymbol{q}\}$ of frequencies having N values of frequency with spacing $1/N\Delta$. Therefore to avoid aliasing we require $1/N\Delta \leq p/2 = k/2q_m z$ or, setting $2q_m = 1/\Delta$:

$$Q = \frac{N\Delta^2 k}{z} \geq 1 \tag{3.35}$$

Thus, we conclude that when Q is greater than unity we can avoid aliasing when using the frequency-space method of defocus propagation. With already established values of N, Δ and k, we may investigate the behaviour of Q as a function of z (which we can see will decay as z^{-1}). Plotting Q as a function of defocus z in figure 3.9, we see that the maximal defocus allowable without aliasing effects present using the frequency-space method is $\approx 6.2\mu m$.

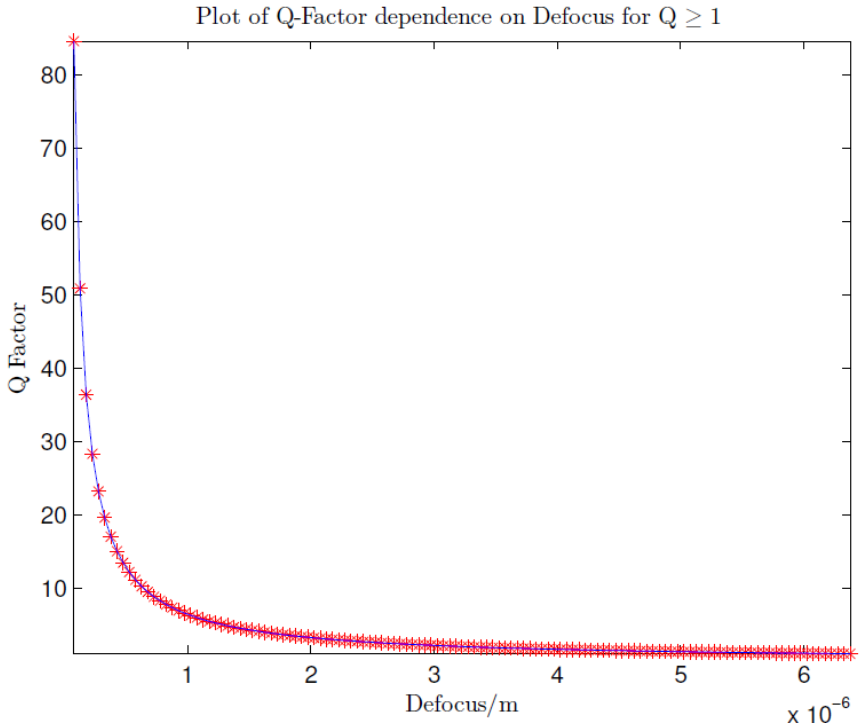

Figure 3.9: Q-factor vs Defocus plot for sufficient sampling of Fresnel propagator

Such defocus results are plotted in figure 3.10, with columns giving coherent field and incoherent intensity results and rows giving successive defocus results, respectively. It is clear that both the coherent and incoherent images evolve with defocus, but there is significant difference in the magnitude of such evolution. The coherent field appears to still modulate fringes regardless of defocus, although the appearance of such fringes does evolve. As the defocus increases, we begin to see secondary fringes appear between successive periods, doubling the image fringe number. By comparison, the incoherent intensity appears to lose fringe contrast much more rapidly, evolving to a uniform field with no fringe modulation for a defocus of $4\mu m$. This indicates that the incoherent imaging setup has a much smaller depth of field, or depth of focus, a startling, yet interesting consequence of a simple alteration of the state of coherence of the illumination and one that will be of paramount importance to the task at hand.

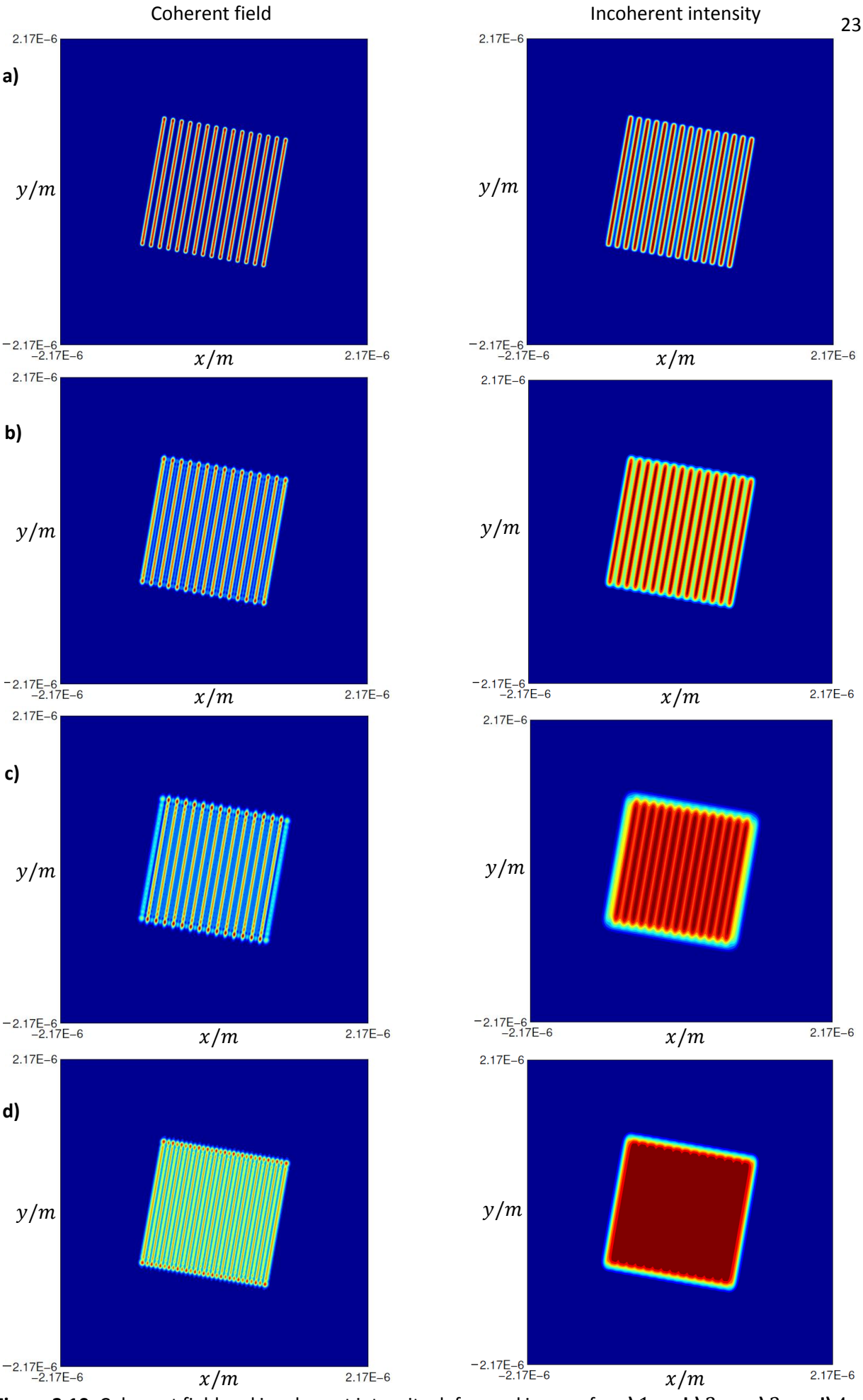

Figure 3.10: Coherent field and incoherent intensity defocused images for **a)** $1\mu m$ **b)** $2\mu m$ **c)** $3\mu m$ **d)** $4\mu m$

4. Advanced Computational Simulation

4.1 X-ray Imaging Setups

Having developed a model framework for imaging using a simple converging lens with a *circ* pupil function, we may now introduce a more complex lens framework. The complexity arises as a result of the difference in focusing optic when dealing with X-rays as opposed to optical wavelengths, as the refractive index of glass is ≈ 1 for X-rays. As a result, a converging optical lens lacks the focusing power it possesses for optical wavelengths when dealing with X-rays; an X-ray beam will pass through almost un-deflected when traversing an optical lens. As such, X-ray lenses rely on the principles of diffraction of the X-ray beam as opposed to refraction, allowing the same phase shift to be imparted by the X-ray lens as the optical lens, a quadratic dependence with distance from the optical axis [30].

The focusing optic used is a Fresnel zone plate (FZP), a device utilising an extension of the Arago spot phenomenon caused by diffraction from an opaque disc. The FZP is a diffraction grating, circular in shape, consisting of a series of concentric rings and slots. The rings are usually metal and roughly equal in width to the slots, being fabricated on a thin membrane such as silicon. The design of a FZP is based upon the idea of superposition of the wavelets emanating from a specific set of zones, such as those that are even-numbered [30]. A simulated depiction of a FZP is displayed in figure 4.1a and 4.1b, with the images showing the opaque (circular ring) and transparent (circular slot) regions from two different viewing perspectives.

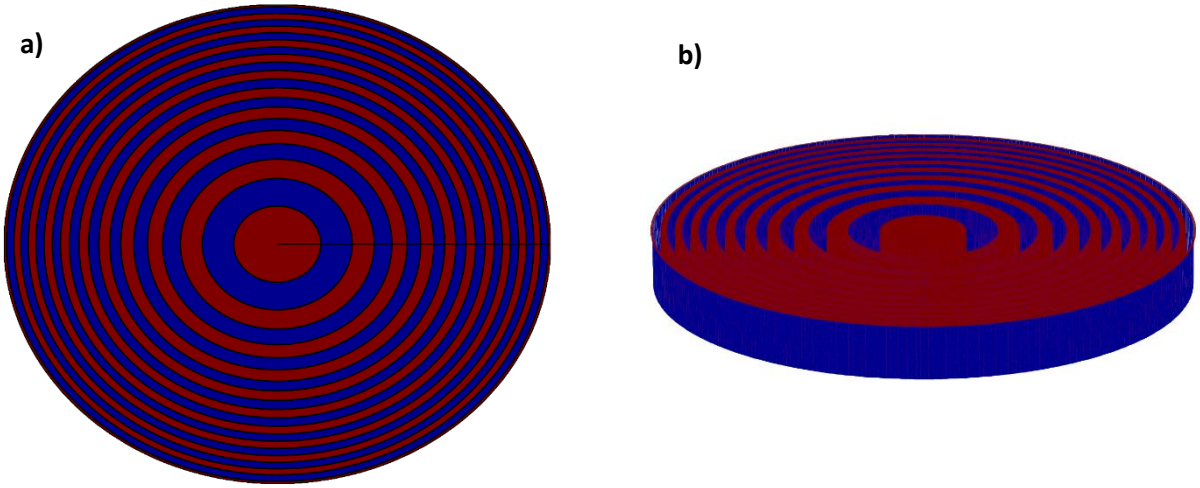

Figure 4.1: FZP alternating ring/slot geometry, viewed from **a)** plan **b)** tilted perspective. Red regions indicate opaque rings, blue regions indicated transparent zones.

One may readily calculate through geometrical arguments the foci positions of the FZP based upon the opaque/transparent periodic structure; there are multiple orders giving multiple foci. As such, one must isolate the particular focus of interest, removing other orders using two components in situ. The first of these is a central stop, required to prevent the zero-order un-diffracted beam from simply passing through the centre of the FZP, as shown in figure 4.1. This alters the pupil function of the lens dramatically, moving from a simple *circ* function to an annulus-shaped function. In addition, an order-sorting aperture (OSA) is used to remove unwanted higher-order diffracted beams [30].

Returning to the chapter 3 simulation, we may introduce a central stop of diameter $D_{CS} = 220\mu m$, yielding a CTF as plotted in figures 4.2a and 4.2b. The outer and inner zone plate diameters are now characteristic of the condenser zone plate (CZP) at TWIN-MIC. In addition to the system CTF we may investigate the corresponding form of the system OTF, in order to achieve an incoherent focused imaging mode, with the OTF calculated from the autocorrelation of the CTF. The OTF is plotted in figures 4.3a and 4.3b.

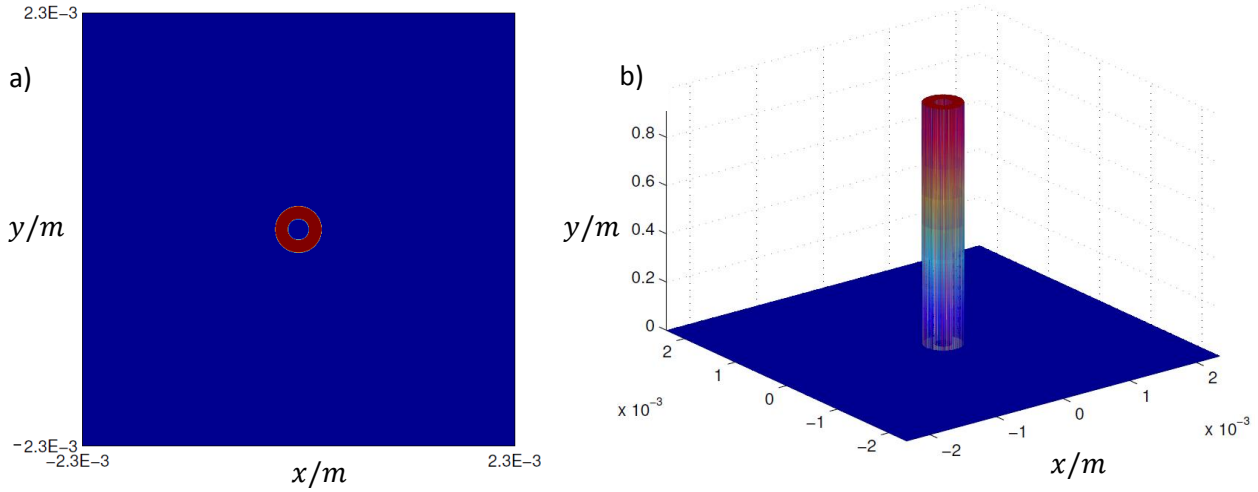

Figure 4.2: a) Contour plot of system CTF **b)** Surface plot of CTF

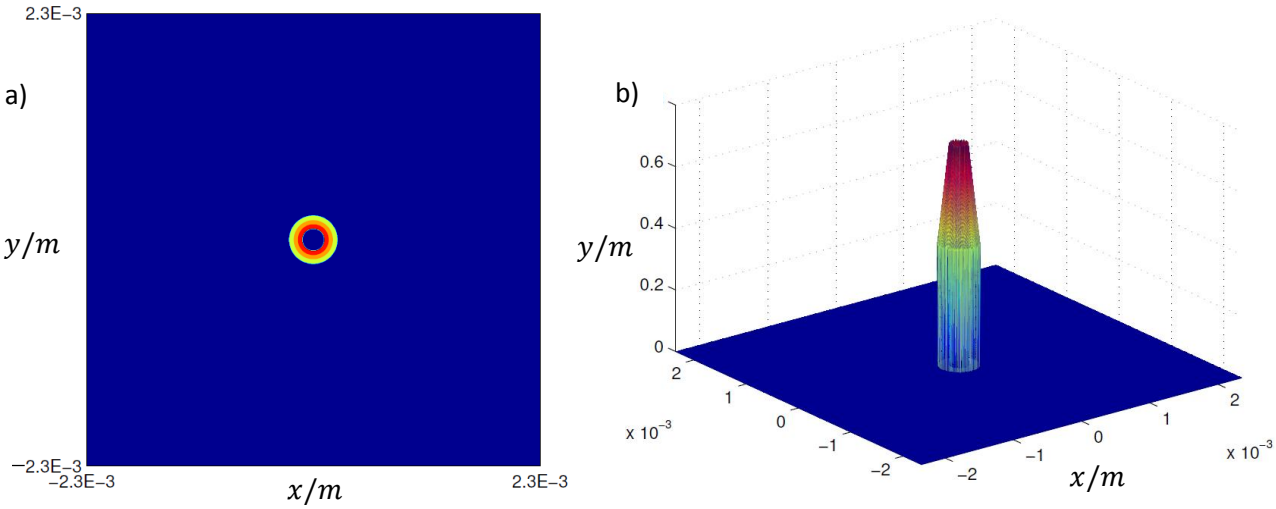

Figure 4.3: a) Contour plot of system OTF **b)** Surface plot of OTF

From figures 4.2a and 4.2b we may appreciate the effect upon the propagating field of the FZP as a result of the central stop located on the optical axis. The CTF acts as a mid-pass filter, preventing both high and low frequencies from being transmitted, with only those within the frequency band between the outer diameter of the FZP and the central stop being transmitted. This leads to interesting alterations to the focused image in both the coherent and incoherent cases, as displayed in figures 4.4a and 4.4b.

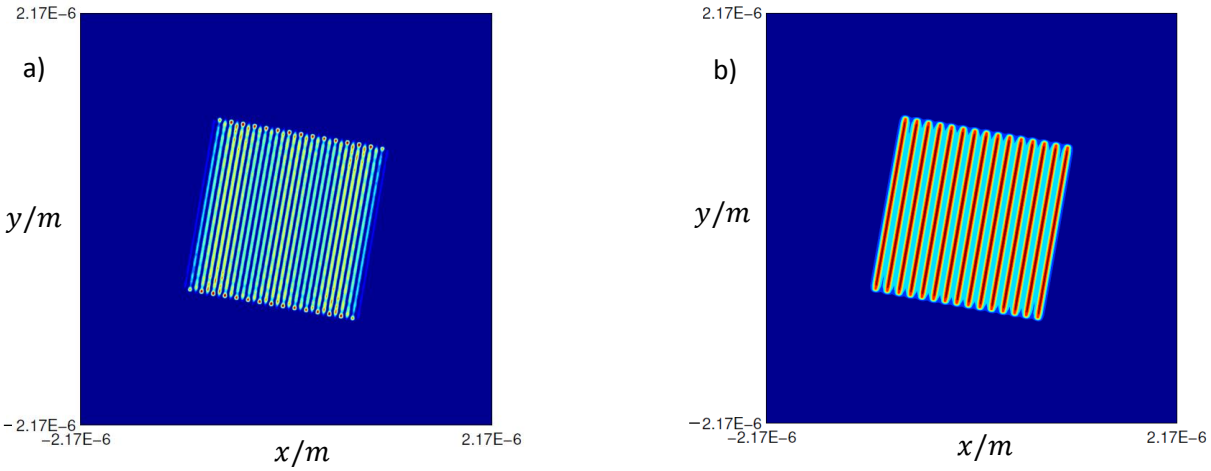

Figure 4.4: a) Focused coherent field **b)** Focused incoherent intensity

We see from figures 4.4a and 4.4b that there are clear differences in the focused coherent field and incoherent intensity upon introducing the central stop for the zone optic. The incoherent

fringes modulate with the same period and approximate width, although are now supported by a non-zero background. The coherent fringes now encompass secondary fringes, doubling the period, with curious Gibbs ringing phenomena present at the fringe ends. The field more closely resembles that of the defocused field in figure (3.10). Finally, the coherent fringes appear to have some higher order low-amplitude modulation, present in the periodic yellow/blue bands in the false colour map.

With the focused imaging setup established using the FZP, we may repeat the procedure described in chapter 3 for the defocusing of the coherent field and incoherent intensity, in order to investigate the depths of focus for coherent and incoherent illumination, and how this may have changed with the introduction of a central stop. Such defocus results are plotted in figure 4.5, with columns giving coherent field and incoherent intensity results and rows giving successive defocus results, respectively.

It is clear that both the coherent and incoherent images evolve with defocus, but there is significant difference in the magnitude of such evolution. The coherent field appears to still modulate fringes regardless of defocus, although the appearance of such fringes does evolve. As the defocus increases, we begin to see additional Gibbs ringing effects at fringe edges and edge artefacts parallel to the fringes appear. By comparison, the incoherent intensity appears to lose fringe contrast much more rapidly, evolving to a uniform field with no fringe modulation for a defocus of $4\mu m$ and above. This indicates that, as concluded for the simpler system case in chapter 3, the incoherent imaging setup has a much smaller depth of field, or depth of focus, whilst the coherent illumination case allows fringes to remain visible at defocus.

4.2 Simulating Incoherence

The formalism laid out so far has dealt with imaging through a lens to a single defocused plane, but we may also then image at successive defocused planes through repeated application of the Fresnel free-space propagator, as described in (2.19). This is straight forward for implementation to propagating fields, but is problematic when dealing with intensity propagation. This is because the square modulus of the propagator must be taken in frequency space, with the product of the square modulus of the frequency-space propagator and the intensity transform taken, and the result inverse transformed to give the propagated intensity. As the propagator in real space takes the form of a complex exponential $e^{i\varphi}$ for some arbitrary phase φ, the square modulus of the propagator is then by definition always equal to unity for all values of φ: $\left|e^{i\varphi}\right| = 1$. Thus, the intensity free-space propagation will have no effect upon the intensity; we must find some other means to propagate in free-space an incoherent field.

As described in chapter 2, an incoherent source is one for which the local phase is continuously random, with the resulting image field phase and amplitude being generally random [25]. Such a source is formed from a superposition of object fields of all local phases. Imagining the source as a finite number of radiators arranged on a grid, as shown in figure 4.6, we see that over a sufficient sampling period, all radiators will have contributed independently, yielding an ensemble average over all possible phases. Of course, the cartoon depiction in figure 4.6 does not give a complete description, as the source-space has been course grained and there exists gaps between source points. As the phase of the field has period 2π, a completely incoherent source could be represented by such a course grained source space, provided the array dimensions extended to infinity. This is to allow a continuous set of phases to be applied to the field, ranging -2π to 2π in both planar dimensions. Alternatively, if the source space was kept of finite dimensions, extending between the limits of -2π to 2π in both planar dimensions, a continuous set of phases could be achieved through infinitesimally fine graining the source space. The results of both setups and their corresponding phase ramping effects are depicted in figure 4.7. Following from this description of an incoherent source, one may see that such a source may be described as a summation over all possible phase-ramped fields:

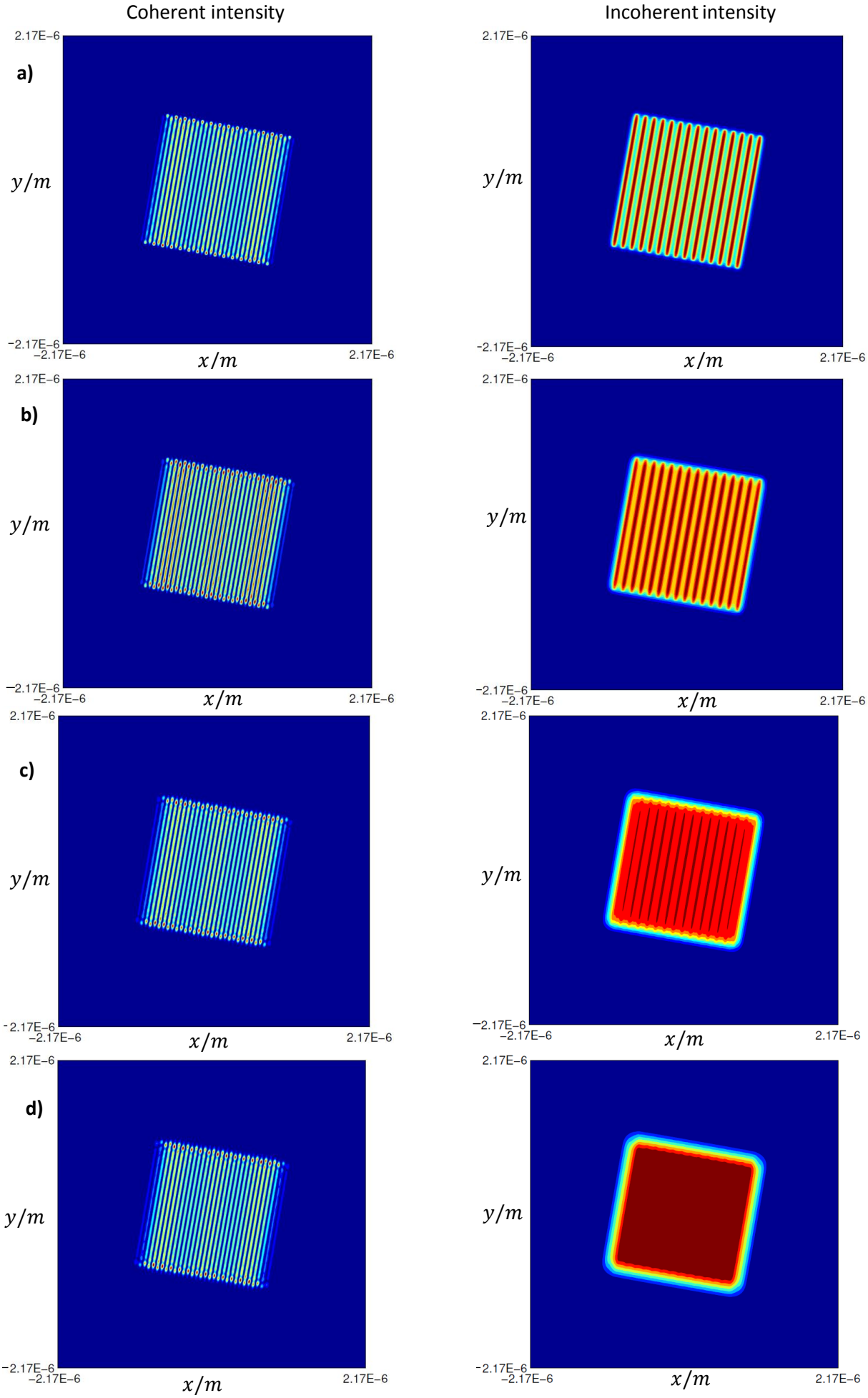

Figure 4.5: Coherent and incoherent intensity defocused images for **a)** $1\mu m$ **b)** $2\mu m$ **c)** $3\mu m$ **d)** $4\mu m$

$$I = \sum_{i=0}^{\infty} |E_i|^2 \tag{4.1}$$

Here, E_i describes the field corresponding to the ith phase ramp. Such a summation is equivalent to the time averaging depicted in figure 4.6, with the averaged random behaviour translated to a step-wise summation, considering all source points independently. In addition, the sum of square modulus terms is taken in order to treat the sources independently, as opposed to the square modulus of the summation of fields, which would introduce coherent interference effects due to cross-product terms.

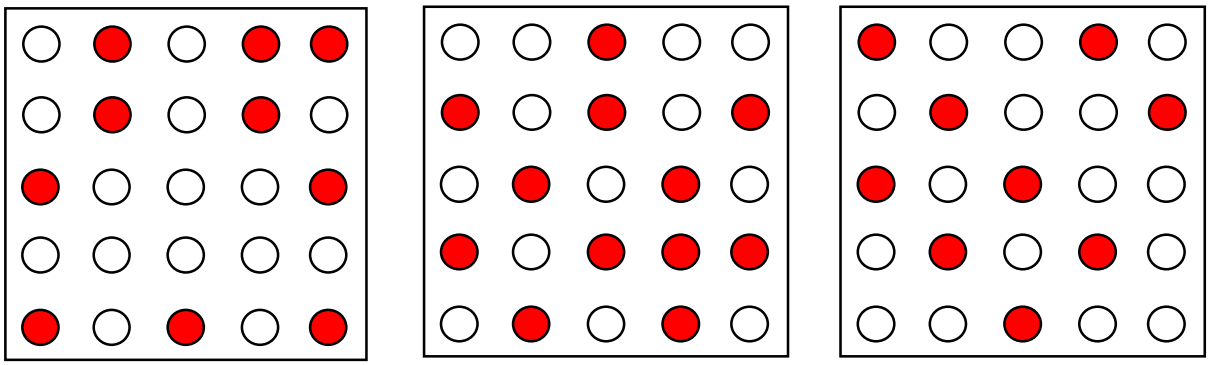

Figure 4.6: Source radiators contributing independently as time progresses, yielding an ensemble average over all possible phases

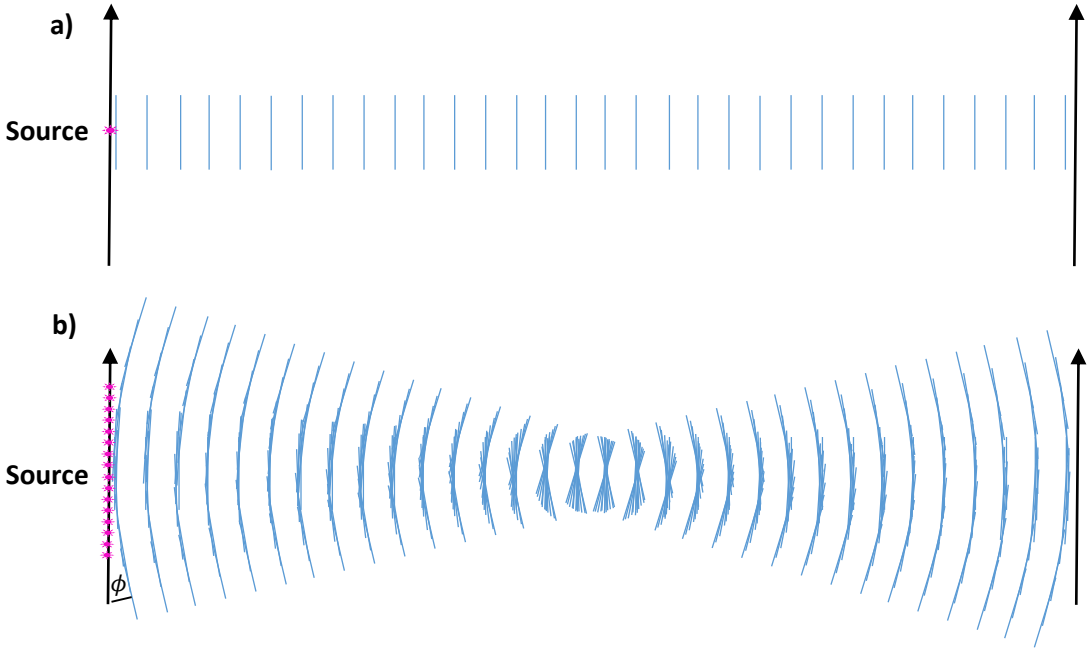

Figure 4.7: a) Single source point with single phase $\phi = 0$ yielding coherent source **b)** Contributions from a number of source points with phases $\phi = -2\pi : 2\pi$ (not all waves shown) in discrete steps, providing better approximation to incoherence. For infinitesimally displaced source points phases yielded are continuous between $\phi = -2\pi : 2\pi$. This is equivalent to a source plane extending to infinity, viewed from a large distance, or of a finite source plane fine-grained to give infinitesimally separated points.

Returning to the issue at hand, that of simulating an incoherent field as opposed to dealing only with an incoherent intensity, we may readily utilise (4.1) in order to construct a model for an incoherent source. Of course, we may never achieve a completely incoherent source using (4.1) as this requires an infinite summation of independent fields. However, we may set the summation limits to some finite value, whereby we may move towards a quasi-incoherent source. Figure 4.7 shows such a process applied to a 1D plane, whilst our simulation necessitates translation to a 2D source array.

We may introduce to our simulation a set of phase ramps, applied to the source field, which will consequently phase-shift the field. Each field is then propagated through the system, and the summation of the square-moduli of the image fields is then taken in order to achieve the incoherent image. This method then allows the free-space propagator to be applied directly to the incoherent field, as with the coherent case, allowing complete modelling of defocus for both coherent and incoherent fields. The phase ramping may be applied with a defined array dimension, determining the fine-graining of the phases applied. For a small set of phase ramps, the source will be highly course-grained, giving a poor model of incoherence. Moving to a larger set of phase ramps, the source will be more fine-grained, giving a better approximation to incoherence. For the computation at hand, the array size is mapped directly to the phase ramp limits applied: the most primitive case of a 3x3 phase ramping routine gives phase ramps displayed in figure 4.8, with limits of $\phi = -2\pi : 2\pi$. For a higher dimensional array, the phase limits are increased in proportion, allowing finer sampling between the $\phi = -2\pi : 2\pi$ limits, due to the periodic nature of the complex exponential.

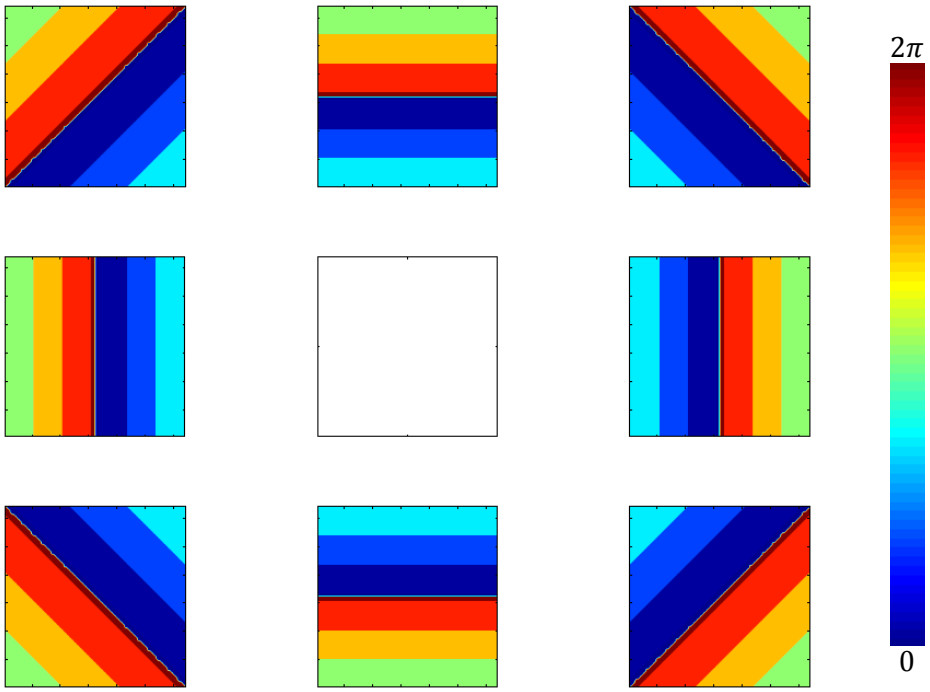

Figure 4.8: Phase ramps applied for 3x3 simulation

Utilising such a method for achieving a quasi-incoherent field, we may investigate the minimum summation size required to replicate results of an incoherent field. To carry out such a test, we use the result of a $4\mu m$ defocus applied to the coherent and incoherent fields shown in figure 4.5 with our more complex system setup. We choose such a defocus value of the approximate depth of focus for incoherent illumination, allowing easy distinguishability between a coherent and incoherent source. Increasing the phase-ramp array size applied, the resulting images are plotted in figure 4.9.

From figure 4.9 it is clear that this method of phase-ramp application and summation over resulting independent source fields moves away from a coherent source and towards an incoherent source, as desired. Following from (4.1), it is clear that as the phase-ramp array size increases, or more formally, the phase space is sampled in a finer-grained method, providing a larger summation, the approximation to incoherence becomes better. For a $4\mu m$ defocus applied we would expect, as indicated by our previous results in figure 4.5, that there should be a complete loss of contrast for an incoherent source, corresponding to the depth of focus, with a coherent source still achieving contrast between fringes. Such a loss of contrast begins to take place at the 31x31 array size, and optimal results begin to set in from a 35x35 array dimension and above, in comparison to figure 4.5. This

increasing in array size replicates the procedure discussed about fine-graining the phase space, or similarly increasing its size to much larger dimensions.

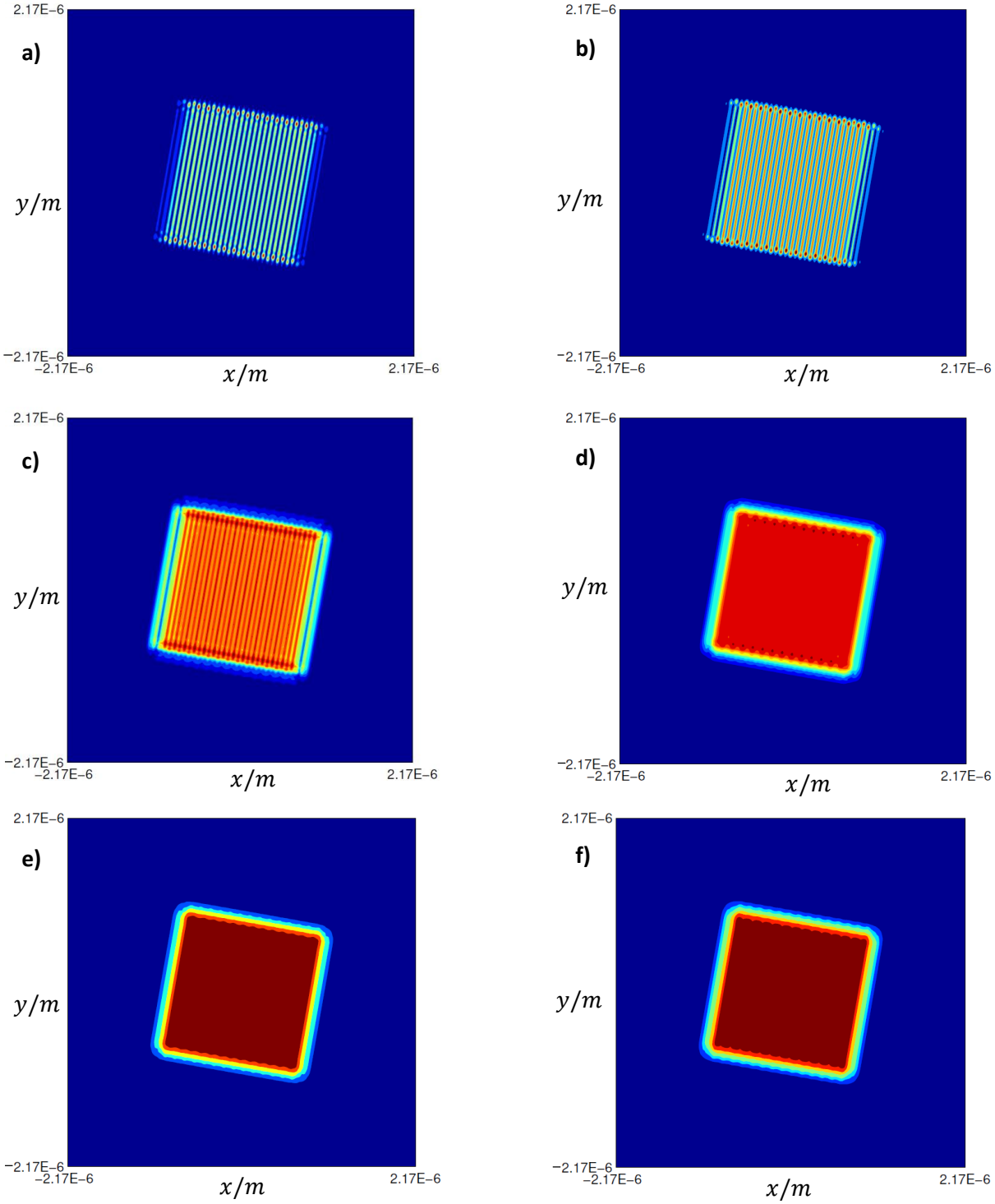

Figure 4.9: Quasi-incoherent $4\mu m$ defocused fringes for phase-ramp array dimensions of **a)** 3x3 **b)** 11x11 **c)** 21s21 **d)** 31x31 **e)** 35x35 **f)** 39x39

Here we have demonstrated that such a procedure does in fact achieve an incoherent source field, allowing us to deal directly with field manipulation as opposed to intensity manipulation, which in turn allows the free-space propagator to be applied to incoherent fields, something impossible to achieve when dealing directly with intensities.

However, what has not been discussed is the need for a compromise between the quality and efficiency of the simulation at hand. In the ideal case of instantaneous simulations, we would envision phase-ramp array dimensions orders of magnitude greater than those applied for figure 4.9. But computational code does not execute instantaneously, instead requiring time for the CPU to execute the code. A compromise must therefore be achieved between the length of time taken for the simulation, and the quality or results obtained. We see from figure 4.9 that once we move above a 35x35 array size, the gains in image quality are minimal. Considering that the base code involved in the phase-ramp application itself requires an average 1.7s rectification time, in addition to the execution time for setting parameters and figure plotting etc., repeating this for 35x35 (1225) realisations gives a total execution time in excess of 0.58 hours for this relatively simple system. We do not wish to add to this already substantial execution time, especially as we will now look to construct our more complex full-system simulation, and so a 35x35 phase-ramp array is utilised to provide the quasi-incoherent source.

5. SIM Imaging with a complete TXM setup

5.1 Complete system simulation

Having established a working model involving a single focusing optic for X-rays, with stout control of the state of coherence of the source illumination, we may finally move to simulating the complete TWIN-MIC system. The TWIN-MIC system represents the common TXM setup, involving a source illumination projected via a CZP to a sample plane, with the transmitted field then projected via a secondary objective zone plate (OZP) to a detector plane yielding the final image [30]. Such a setup is depicted in figure 5.1.

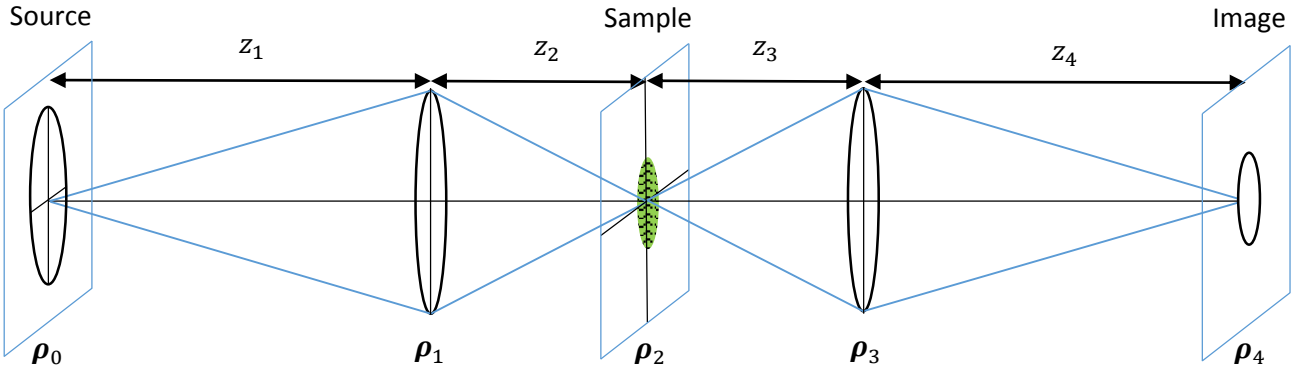

Figure 5.1: Illumination configuration of SIM imaging. Plane $\boldsymbol{\rho}_0$ contains an illumination source, propagating a distance z_1 to a converging lens located at plane $\boldsymbol{\rho}_1$ which then focuses the illumination onto the sample, located at plane $\boldsymbol{\rho}_2$, a further distance z_2 away. The illuminated sample transmission beam then propagates a distance z_3 to another converging lens located at plane $\boldsymbol{\rho}_3$, which finally focuses the beam to a detector located a distance z_4 away at the final image plane $\boldsymbol{\rho}_4$.

In order to model the system completely, an additional field propagation through the OZP to a final image plane is required, repeating the simulation procedure already established. The length parameters z_3 and z_4 are again taken from the TWIN-MIC setup, with $z_3 = 3mm$ and $z_4 = 4m$. In addition, the OZP has focal length $f = 3mm$, outer diameter $D = 250\mu m$ and central stop diameter $D_{CS} = 110\mu m$. The corresponding OZP CTF is displayed in figures 5.2a and 5.2b respectively.

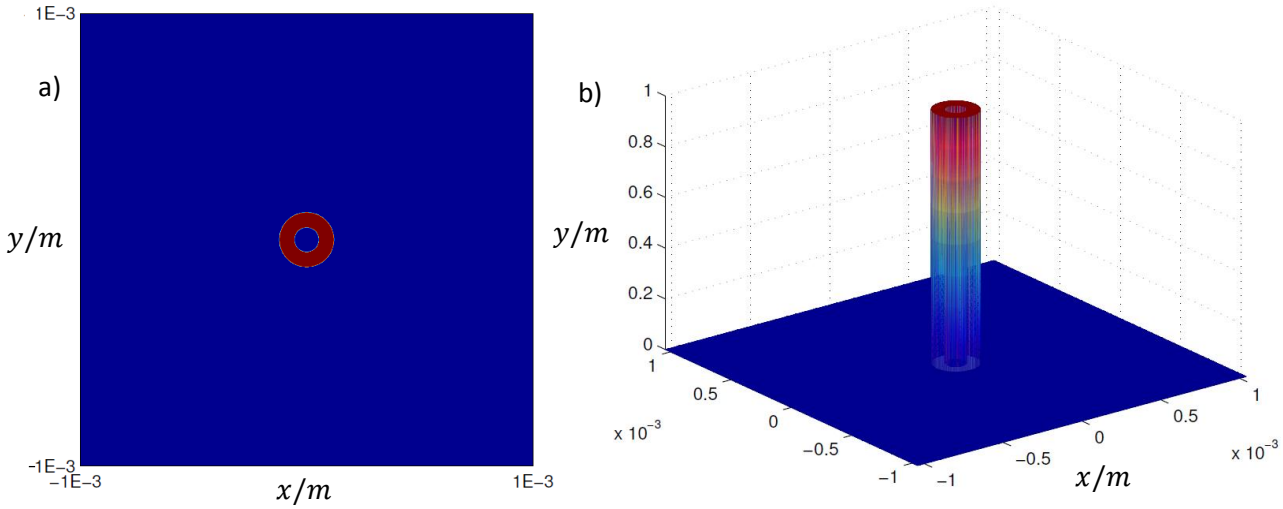

Figure 5.2: a) Contour plot of OZP CTF **b)** Surface plot of OZP CTF

The imaging process as depicted in figure 5.1 may therefore be divided into a number of steps, of which the main components have already been robustly simulated. We require a source pattern to be projected onto a sample, the transmission profile of the sample imprinted onto the intermediate field and the resulting field product projected to the imaging plane. The initial and final projections of the source field to sample and sample field to detector may be carried out using a repeated procedure identical to that already established. In addition, we must consider the auxiliary steps involved for the transmission profile effect of the sample. Continuing with our fringe source, we may readily obtain coherent and incoherent source illumination images using the new setup as shown in figure 5.1, with the results shown in figure 5.3.

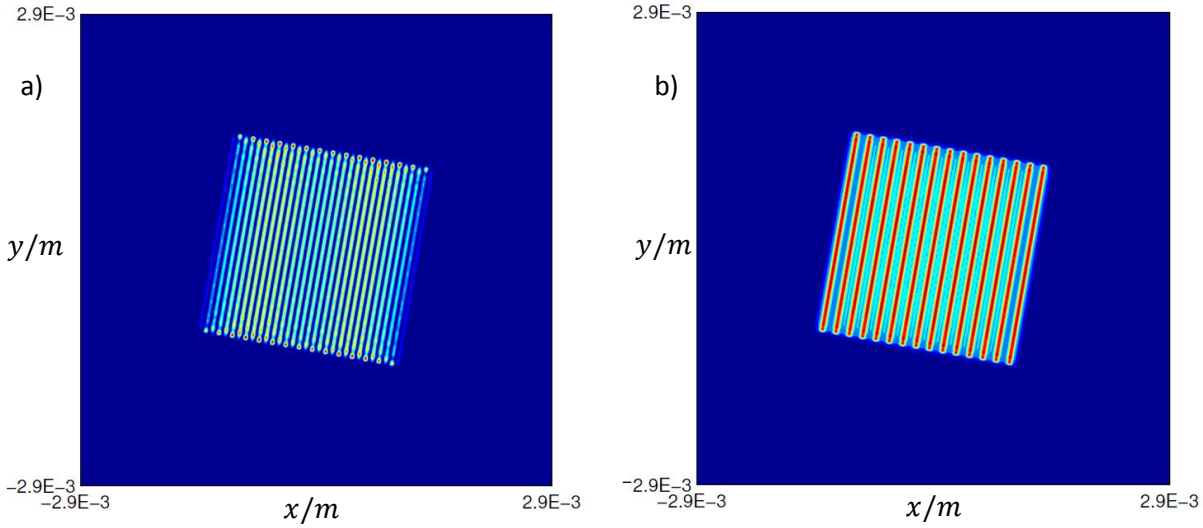

Figure 5.3: a) *A* transmission object **b)** *B* transmission object

As we are investigating an imaging technique for achieving 3D images using a 2D setup, we must correspondingly construct a 3D sample using a series of 2D amplitude transmission profiles located at various axial distances. Such a sample may then in principle be moved through the focus of the setup, allowing successive axial slices to be imaged and a reconstruction image of the 3D object obtained.

To begin with, we may discuss the 3D simulation object. We limit ourselves to three transmission objects for simplicity, with the profiles taking the form of the characters *A*, *B* and *C.* The characters themselves have a constant transmission profile of 0.5, meaning that the field incident at the character locations has an amplitude reduction of 50%. The three characters are located at various positions in the applied array, as shown in figure 5.4, for ease of discernment in the final image.

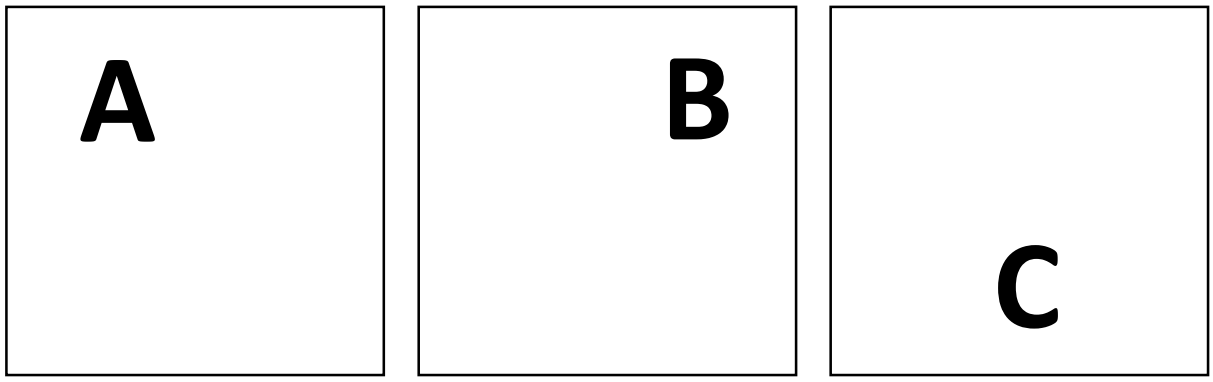

Figure 5.4: *A, B and C* transmission objects

The transmission objects themselves are arranged as shown in figure 5.5, with *A* being closest to the source, followed by *B* and then *C*. The objects are equidistant, separated by some distance δz, as shown in figure 5.5. We may begin imaging with *B* located at focus, with δz incremented from $0\mu m$

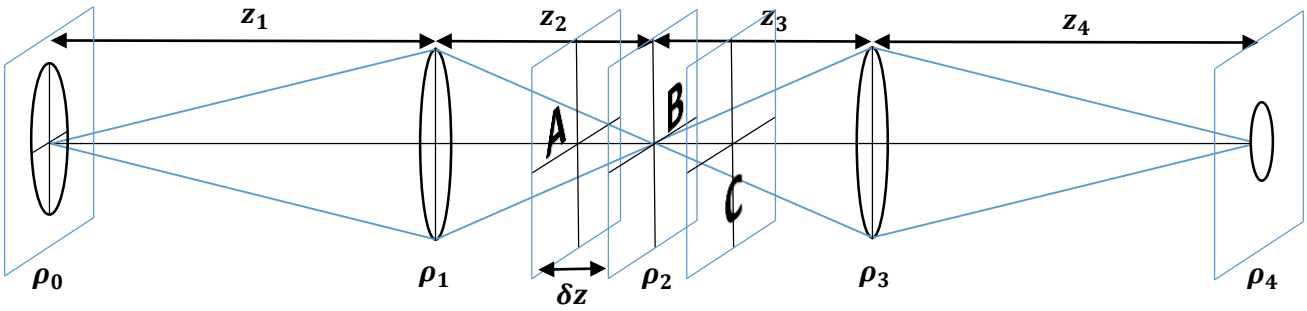

Figure 5.5: Complete imaging setup for 3D sample consisting of equidistant transmission objects

in $1\mu m$ steps, whereby the *A* and *C* will move successively out of focus. At each stage we image both with coherent and incoherent illumination, with results showing successive $2\mu m$ displacements plotted in figure 5.6.

We see from both the coherent and incoherent results that, as the equidistant spacing is increased, the A and C objects begin to lose contrast, much more rapidly in the incoherent case, as is to be expected. We see in fact that our earlier estimates of a depth of focus $4\mu m$ is again confirmed here, with some minor artefacts still present at such a defocus and above. For the coherent case, we see that although the out-of-focus objects have a loss of contrast, this does not increase in magnitude as much as the incoherent case. In addition, a peculiar phenomenon arises with the coherent case by which the out-of-focus shapes appear as a double image, translated left and right of centre. This peculiarity arises as a result of the form of the CTF, whereby the zero-order beam is removed due to the ZP central stop, removing the central part of the out-of-focus shapes, leaving an apparent double image. This was confirmed from additional simulations not included in this report due to size constraints.

5.2 SIM Imaging via phase-stepping algorithms

We have now demonstrated that using an incoherent fringe-projection setup allows a smaller depth of focus to be achieved with the imaging system, benefiting resolution in the z direction. However, we are still left with the issue of our final image having a periodic modulation overlay in the form of the fringe pattern. In order to obtain a complete axial slice of the sample some method of removal of the fringes must be implemented. The method of removal that may be implemented involves the application of a successive phase-stepping algorithm to the projected fringes in order to extract an un-modulated final axial slice, which we may refer to as the SIM image [2]. The principle of translation of sample fringes is readily achieved via translation of the source fringes, as in figure 5.7 which, with a grating acting as the fringe source, is accomplished via a well-defined phase shift applied to the grating.

We may consider a general K-step technique involving a circular phase sequence, $\phi_n = 2\pi n/K$ where n increments from 0 to $K-1$. We may then isolate an un-modulated image using:

$$I_{SIM} = \frac{1}{K}\sum_{n=0}^{K-1} e^{i\phi_n} I^{(n)} \tag{5.1}$$

The phase-stepping algorithms of interest to SIM generally operate with $K = 4, 5$ [31] although any step technique may be adopted provided that the steps are controllable and well defined. We wish to utilise a phase-stepping algorithm that is both computationally efficient and proficient at removing unwanted artefacts. We therefore desire a low value of K in order to reduce the number of realisations of code required, as each successive phase step requires an additional realisation. In addition, phase-stepping routings with $K = 5$ have been shown to be most beneficial in removing artefacts [31]. Beginning with $K = 4$, we have:

$$I_{SIM} = \frac{1}{4}\left[\left(I^{(0)} - I^{(2)}\right) + i\left(I^{(1)} - I^{(3)}\right)\right] \tag{5.2}$$

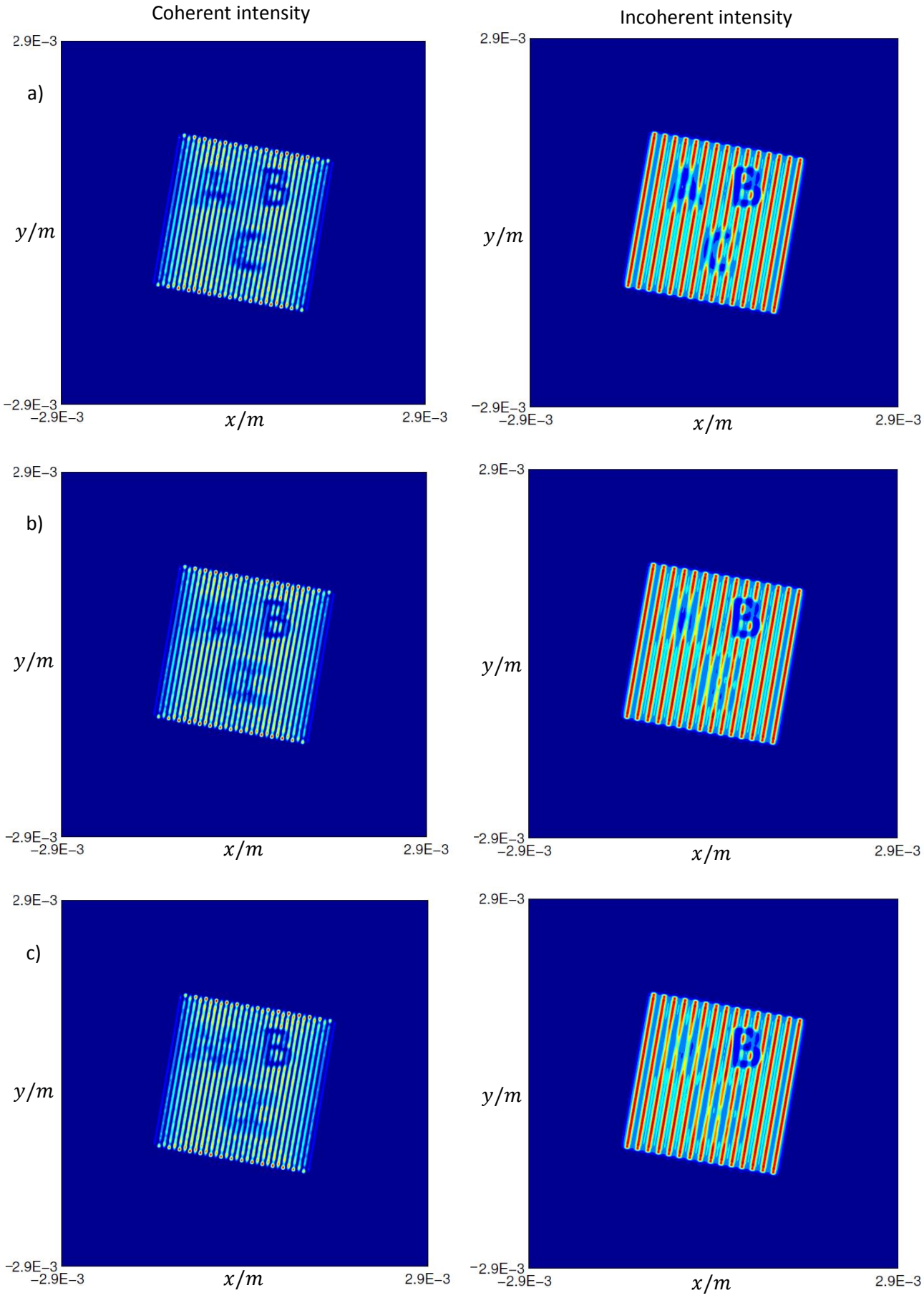

Figure 5.6: Coherent and incoherent intensity 3D sample images for **a)** $2\mu m$ **b)** $4\mu m$ **c)** $6\mu m$ equidistant distance between A – B and B – C objects respectively

Applying such a routine to both the coherent and incoherent images already depicted in figure 5.6 for a range of equidistant defocus values, we may obtain a final SIM image free from fringe modulation. Such results are plotted in figure 5.8 for the respective equidistant defocus values for both the coherent and incoherent illumination cases.

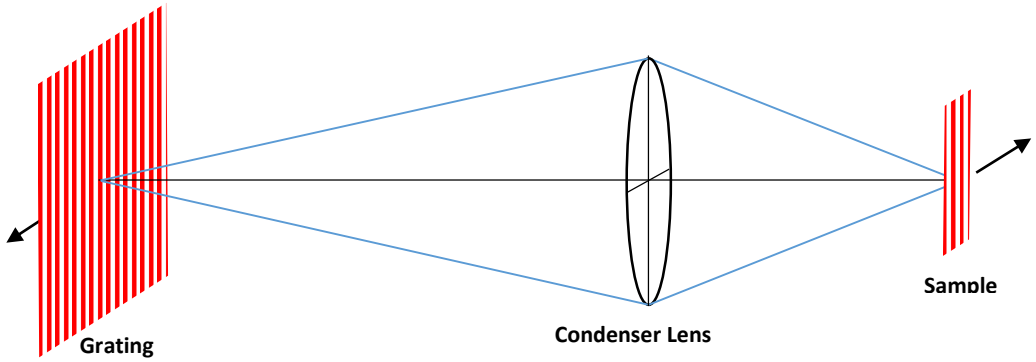

Figure 5.7: Fringe projection translation via grating translation

From figure 5.8 we observe that the phase-stepping algorithm bares no benefit to the coherent illumination case, resulting in near-complete cancellation of the successive images, with some edge artefacts remaining as a result of the fringe translations away from centre. In the case of incoherent illumination we see that the focused *B* object is well resolved in all cases, with the out of focus *A* and *C* objects rapidly losing contrast and magnitude of absorption as the equidistant spacing is increased. In addition, the fringe modulation has been removed to leave an almost uniform background with some minor artefacts present as a result of the transmission objects themselves. In addition, there are large parallel peaks in the background at the image edges due to the translation away from centre of the successive images, appearing as the red parallel stripes at the image edge. One might expect even better removal of the poorly resolved A and C shapes at each defocus level, particularly as it has been demonstrated in the case of fringe modulation that the system depth of focus is approximately $4\mu m$.

We may, as a check, implement the 5-step phase-stepping algorithm in order to determine whether better results are obtained using such a technique. Comparing for the $6\mu m$ equidistant spacing we see in figure 5.9 that results for the 4-step and 5-step algorithm appear almost identical. We conclude, therefore, that the phase-stepping routine is not at fault, and that this is simply the behaviour of the system. We would, of course, likely achieve more desirable results upon introducing more modes into the incoherence simulation, at great loss to the computational efficiency. In addition, a more powerful computing effort would allow for a greater number of fringes to be sampled with equivalent precision, facilitating a more detailed out-of-focus rejection in the SIM image.

It must be remembered that the computational model constructed is not the system of study itself, but namely a model constructed to demonstrate that such a SIM technique might be feasible with such a setup. Having confirmed the validity of the technique, we may conclude that such an experimental effort is entirely viable, although presents its own engineering challenges in achieving the required illumination in order to facilitate SIM imaging. Such experimental efforts will be discussed briefly in the next chapter.

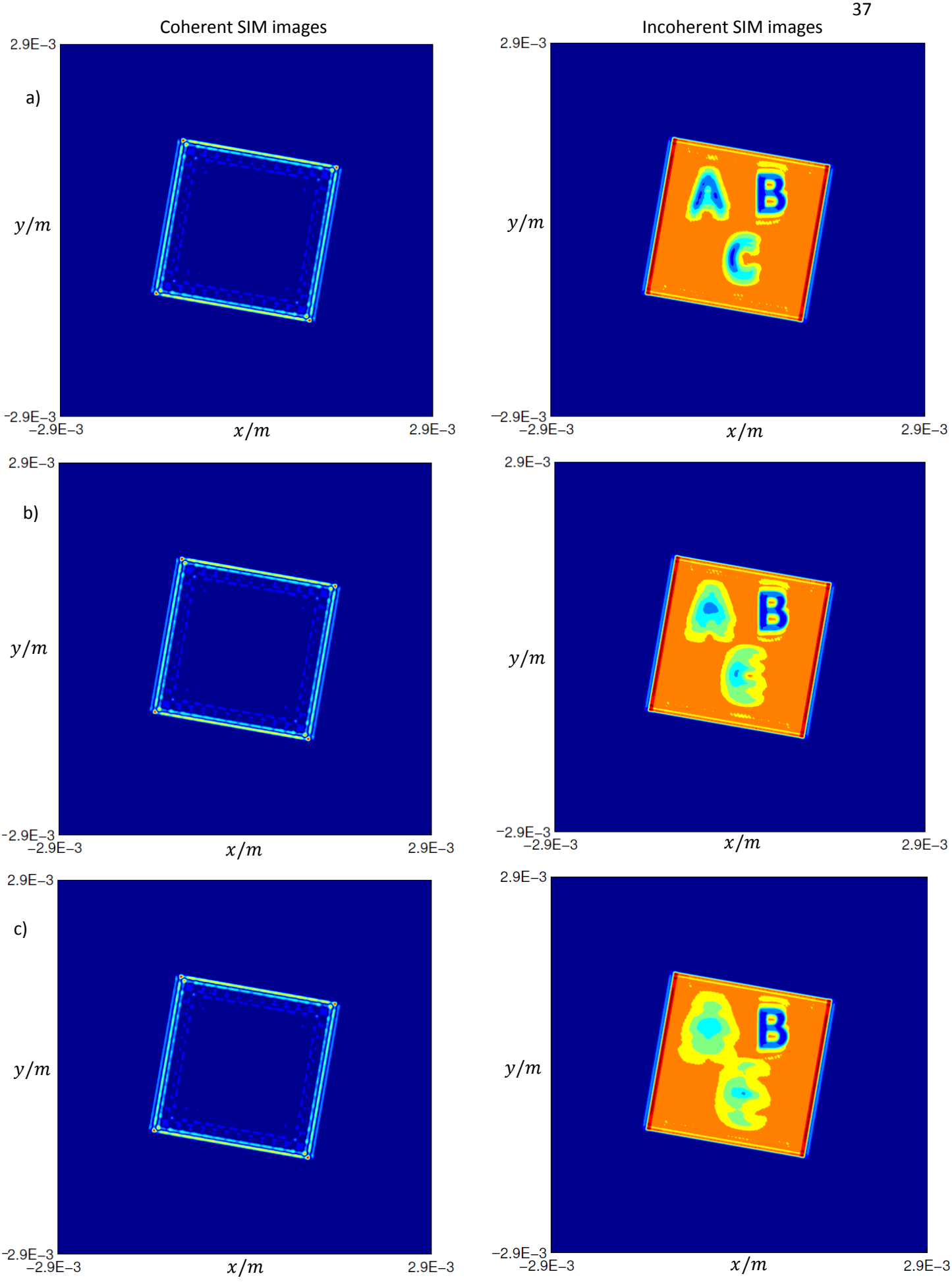

Figure 5.8: Coherent and incoherent 4-step SIM images for **a)** $2\mu m$ **b)** $4\mu m$ **c)** $6\mu m$ equidistant distance between A – B and B – C objects respectively

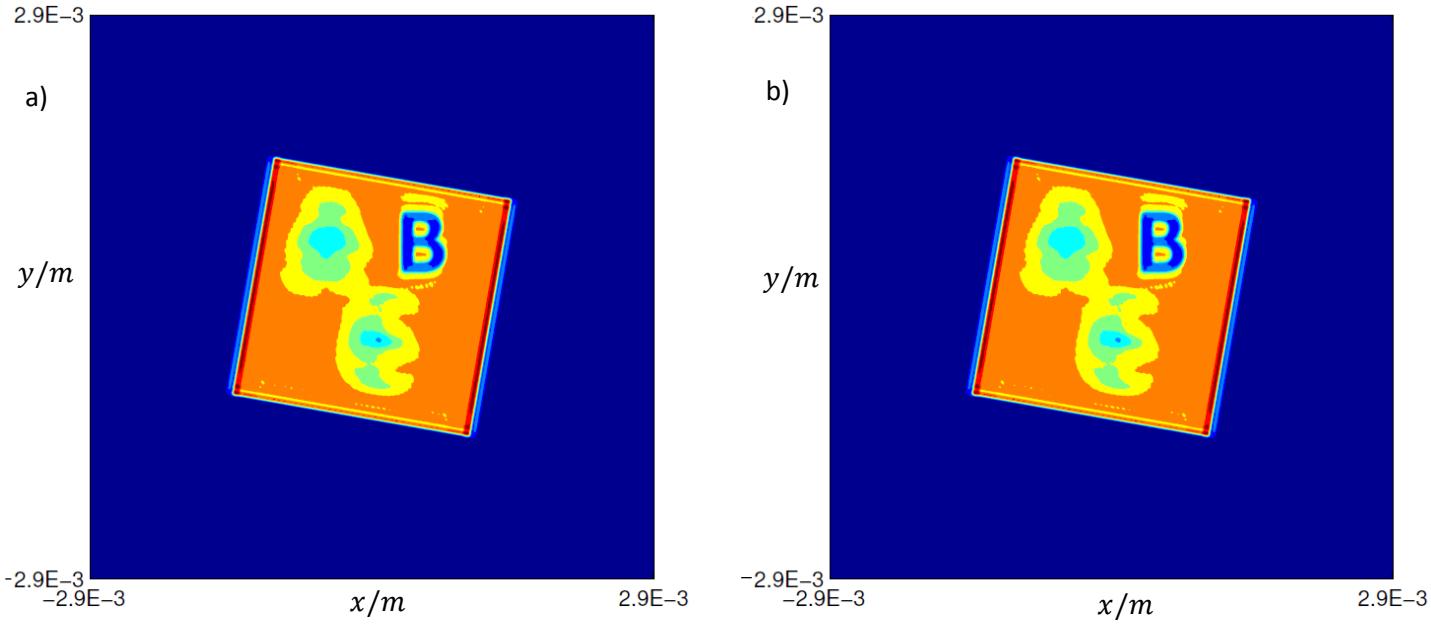

Figure 5.9: a) Incoherent 4-step SIM **b)** Incoherent 5-step SIM images for $6\mu m$ equidistant distance between A – B and B – C objects respectively

6. Experimental Attempts at X-ray SIM

6.1 Elettra System

Here we will briefly discuss the attempts made in December 2013 to achieve experimentally a SIM mode of imaging using the TWIN-MIC TXM setup, as depicted in figure 5.5.

The experimental system itself is designed to allow the mounting of many closely spaced components using a series of concentric cylindrical hollow mounts, as depicted in figure 6.1a. Such mounts are coupled to moveable stages which may translate in all three spatial dimensions. The successive components are then combined in the concentric format shown in figure 6.1b, allowing the independent movement of components at very confined lateral spacing. In addition, we see in figure 6.1b the arrangement of components upstream from the sample, where the sample itself is located between two vacuum seals separating the main experimental enclosures. The enclosures themselves are held under high vacuum due to the short range of the soft X-rays used in air.

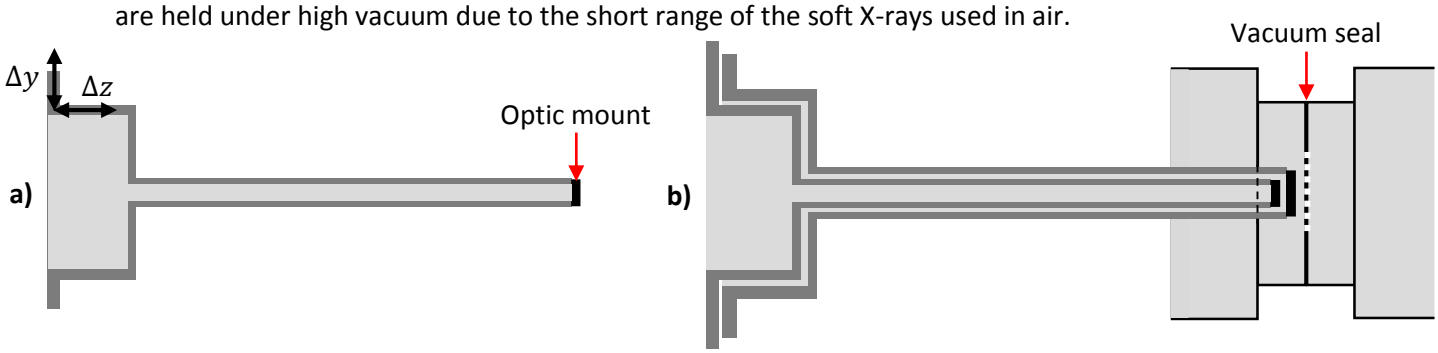

Figure 6.1: a) TWINMIC stage mount **b)** Concentric stage mounts and sample vacuum seal arrangement

Figures 6.2a and 6.2b show the experimental mounting stage and motor stage to which it is attached in order to allow three-axis movement via piezo motors. Figures 6.3a and 6.3b show the concentric arrangement of such mounting stages as depicted in figure 6.2b. We see in figures 6.4a and 6.4b the sample chamber located between enclosures in the open and closed positions, as depicted in figure 6.1b. Finally, we see in figure 6.5 the TXM CCD located downstream from the post-sample enclosure.

Having described the key components and setup of TWIN-MIC, we now move on to discuss the modifications required in order to operate in a SIM mode, as required. The most important alteration comes in the state of coherence of the illumination. The beam provided to TWIN-MIC is a monochromatic, highly-coherent beam, as a result of the mechanisms of emission within the Elettra synchrotron itself and secondary beam tuning devices located upstream from the main system, including toroidal focusing mirrors and monochromator devices [30].

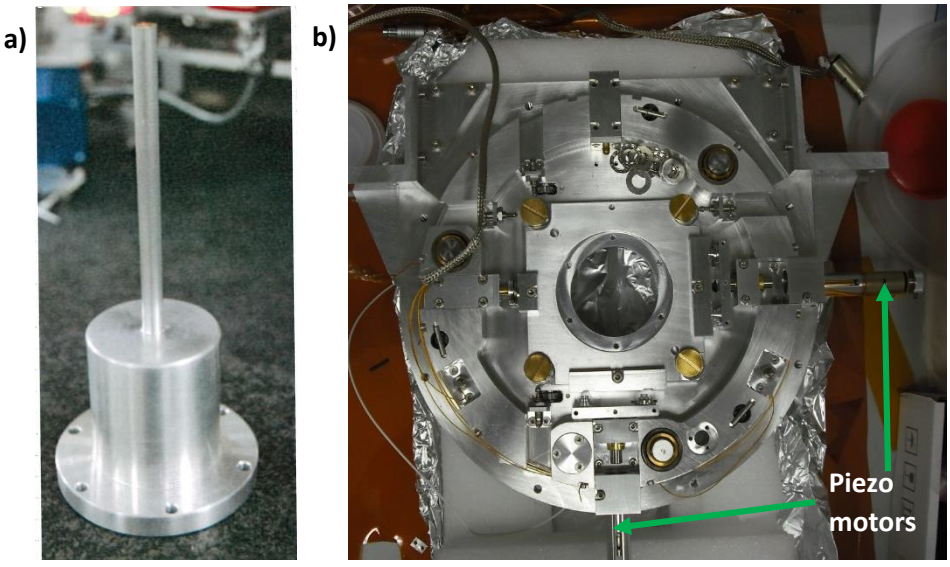

Figure 6.2: a) TWINMIC stage mount **b)** Motor stage

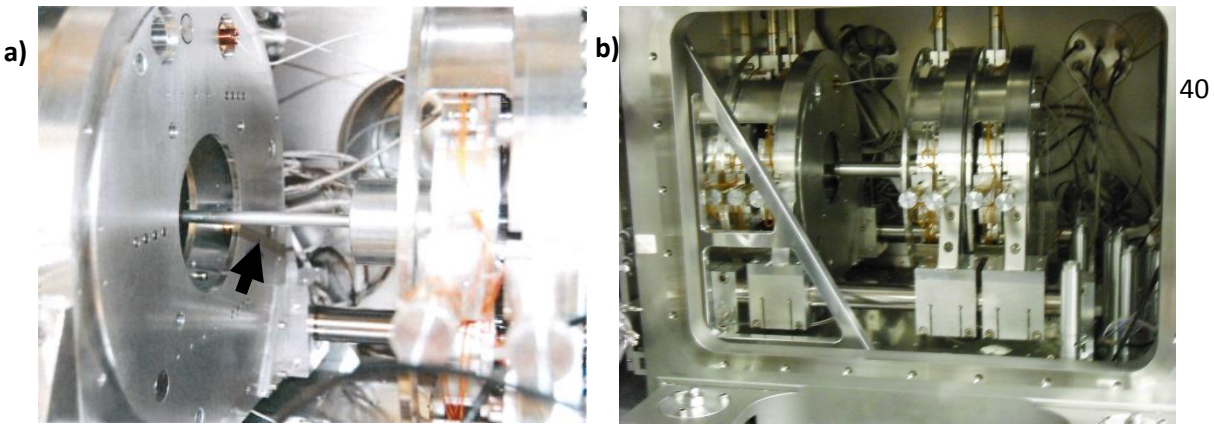

Figure 6.3: a) Close up stage mount in enclosure **b)** Multiple concentric stages in enclosure

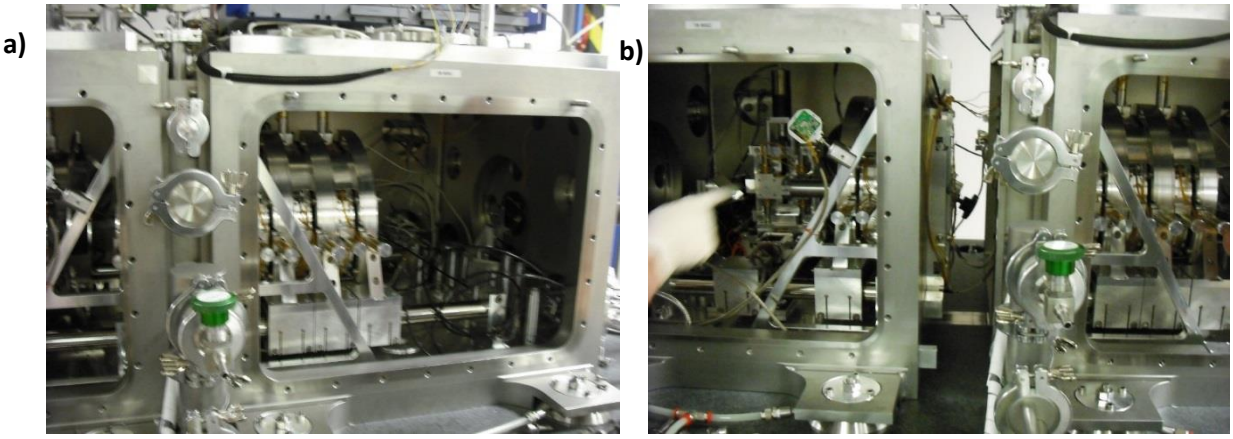

Figure 6.4: a) Closed sample chamber and enclosures **b)** Vacuum seal open for sample mounting

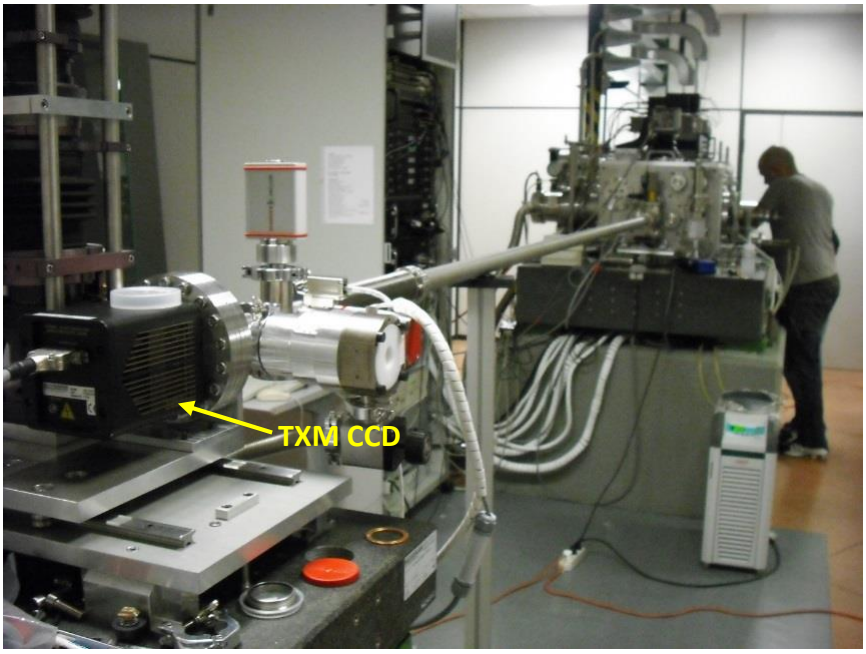

Figure 6.5: TXM CCD stage providing final system image

For SIM imaging, such a coherent beam must be altered in order to achieve a highly incoherent source of illumination, as has already been described and demonstrated computationally in previous sections. In order to achieve such incoherence experimentally, a similar method to that employed computationally is introduced, namely the independent summation across all source points. Of course, such a method is altered somewhat, but still follows the same fundamental principles of independent radiator summation. A moveable diffuser, as depicted crudely in figure 6.6, is introduced to the beam, with the diffuser formed from a random etching of pinholes into an opaque substrate.

Allowing the diffuser stage to trace out a scan in the x and y dimensions during imaging, the individual pinholes act as independent radiators, with no temporal or spatial coherence, following the general protocol laid out in the computational model; a highly incoherent beam may be obtained. Figure 6.6 shows the mounted diffuser stage. In addition to the need for incoherent illumination, we require a fringe illumination to be projected onto the sample in order to achieve a SIM mode of imaging. Such an illumination pattern is achieved via the imaging of a diffraction grating object in the system, with the sample located at the focused image plane, as has been the case for the computational simulations.

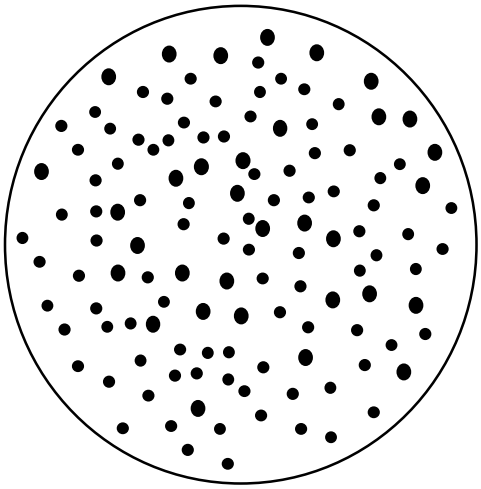

Figure 6.5: TXM CCD stage providing final system image

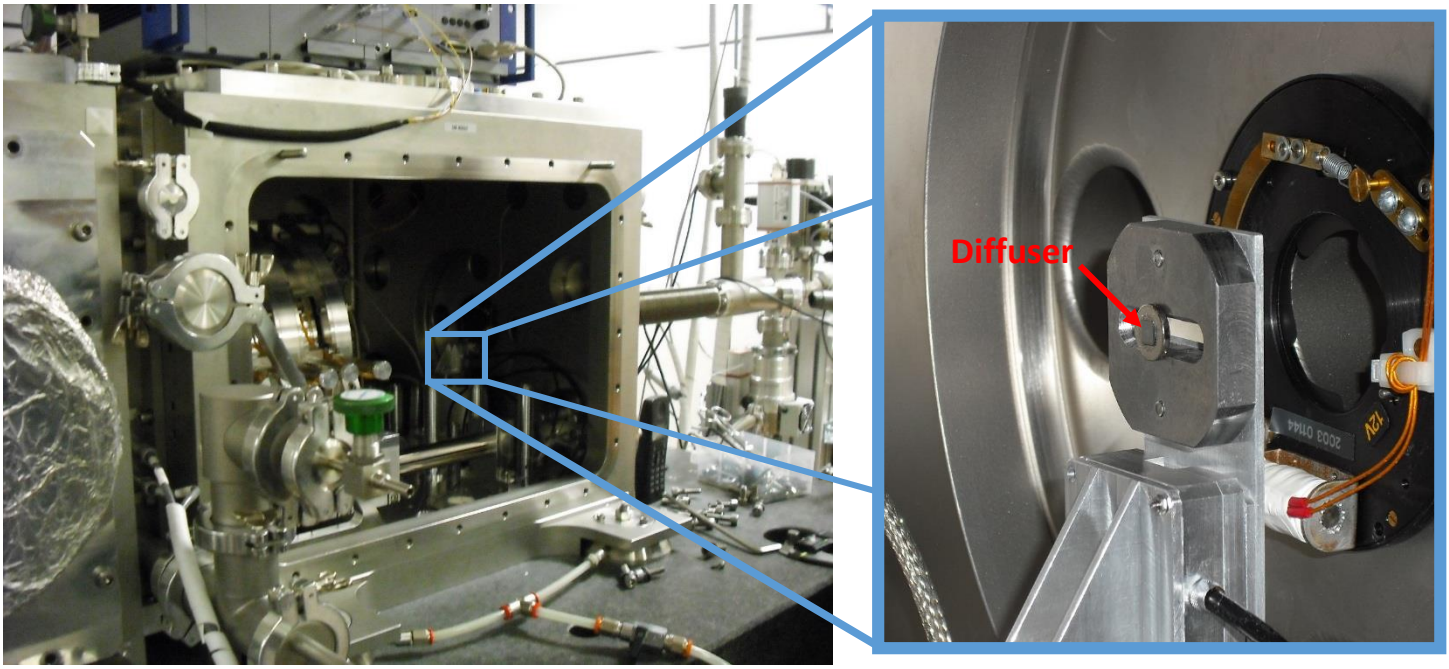

Figure 6.6: Mounted diffuser stage and diffuser optic

6.2 Experimental Results

Although the diffuser and stage were mounted successfully, along with the other necessary optics including the CZP, OZP and grating, several issues were encountered during the experiment. Many components required initial installation, location and alignment time; Making adjustments to the setup is costly as the high-vacuum environment necessitates a gradual re-pressurisation and de-

pressurisation following system alterations, taking several hours for modifications to be made. Also, one of the lateral motors failed without replacement on the diffuser stage during the experiment, reducing the incoherence of the source to only one dimension. Finally, there were several engineering issues faced including the incorrect milling of pinhole stages and other components by the beam-line technician, along with the absence of the beam-line technician for part of the week. In summary, there were numerous issues faced in carrying out the experiment, resulting in inconclusive results.

The experiment concluded with the system having operated in a TXM setup with diffuser present, providing incoherent TXM images. The components installed during the experiment will remain, ready to be used upon return to TWIN-MIC in May 2014. More conclusive results are expected for the next experimental visit, in part due to the large amount of groundwork laid during the December 2013 visit, along with updates to the TWIN-MIC scripting software to allow for better control and driving of the system.

7. Conclusions

The aim of this project was to investigate the ability of a TXM setup to achieve optical sectioning of a thick sample via implementation of a SIM mode of imaging. The project was multi-faceted insomuch as it involved both the computational simulation of such a system, coupled with an attempted experimental verification.

The computational simulation attempts demonstrated a clear ability for such a TXM setup to achieve optical sectioning using some simple sample objects, with the necessity of incoherent illumination for such a SIM mode of imaging to operate also clearly demonstrated. Out-of-focus axial planes showed clear rejection at small defocus values, with simulations for $4\mu m$ equidistant planes and above yielding noteworthy rejection power. In addition, a quasi-comparison to a standard TXM mode of imaging indicated gains in depth resolution when using a SIM imaging mode. The code itself was developed with the upmost necessity of accurate results, coupled with the requirement of computational efficiency. Various phase-stepping algorithms were implemented, with the most robust and efficient four- and five-step algorithms compared; the four-step algorithm was implemented in order to reduce execution times by approximately 20%, along with its accuracy when compared to the most accurate five-step algorithm.

The experimental visit to Elettra in order to attempt a SIM mode of imaging using the TWIN-MIC TXM suffered from its own set of drawbacks, namely engineering issues in establishing a working setup. Key issues included the failure of a motor on the diffuser stage, coupled with issues in mounting and locating objects such as the grating. These issues were only exacerbated by the lengthy de- and re-pressurising of the high vacuum system. The visit did, however, allow for the mounting of the diffuser stage and achievement of a TXM mode of imaging using incoherent light.

In conclusion, the computational simulation was successful in its purpose of verifying that a SIM mode of imaging is indeed achievable using a source of X-rays via a TXM as opposed to a common optical-wavelength setup. To improve on the model, an enhanced, quantitative comparison between coherent/incoherent illumination cases in the SIM and non-SIM modes of imaging could be attempted, in addition to higher-order incoherence simulations attempted on a more powerful machine, along with a finer sampling of fringes to provide more precise removal of the modulating fringes. The experimental attempt was not entirely successful, although was able to make some vital progress which will in no doubt be beneficial for future attempts at repeating the experiment, where a complete demonstration of X-ray SIM is anticipated.

8. References

[1] Epstein, M. *et al. "Morphological and Biological studies on a virus in cultured lymphoblasts from Burkitt's lymphoma"*, J. Exp. Med. **121**, pp. 761 – 770 (1965)

[2] Neil, M., Juškaitis, R. and Wilson, T. *"Method of obtaining optical sectioning by using structured light in a conventional microscope"*, Opt Lett. **22**, pp. 1905-1907 (1997)

[3] Neil, N., *et al.*, *"Wide-field optically sectioning fluorescence microscopy with laser illumination"*, J. Microsc. **197**, pp. 1-4 (1999)

[4] Wilson, T. *"Optical sectioning in fluorescence microscopy"*, J. Microsc. **242**, 111-116 (2010)

[5] Neil, M., Juškaitis, R. and Wilson, T., *"Optically sectioned images in widefield fluorescence microscopy"*, Proc. SPIE **3261**, pp. 4-6 (1998)

[6] Karadaglić, D. and Wilson, T. *"Image formation in structured illumination wide-field fluorescence microscopy"*, Micron **39**, pp. 808-818 (2008)

[7] Conchello, J. and Lichtmann, J. *"Optical sectioning microscopy"*, Nat. Methods **2**, pp. 920 – 931 (2005)

[8] Chasles, F., Debertret, B. and Boccara, A. *"Optimization and characterization of a structured illumination microscope",* OpEx **15**, pp. 16130-16140 (2007)

[9] Petran, M. *et al.*, *"Tandem–scanning reflected-light microscope"*, J. Opt. Soc. Am. **58**, pp. 661-664 (1968)

[10] Sheppard, C. and Mao, X. *"Confocal microscopes with slit apertures"*, J. Mod. Opt. **35**, pp. 1169-1185 (1988)

[11] Wilson, T. and Sheppard, C. "*Theory and Practice of Scanning Optical Microscopy"*, Academic London, (1984)

[12] Neumann, B. Proc. SPIE **1139**, pp. 102 (1989)

[13] Morgan, C. *"Optical sensor for imaging an object"*, U.S. patent 5, **381**, pp. 236 (January 10, 995)

[14] Křížek, P., Raška, I. and Hagen, G. *"Flexible structured illumination microscope with a programmable illumination array"*, Opt. Expr., Vol. 20, Issue 22, pp. 24585-24599 (2012)

[15] Nelson, J. *et al.*, *"High-resolution x-ray diffraction microscopy of specifically labelled yeast cells"*, PNAS **107**, pp. 7235-7239 (2010)

[16] Woodford, O. (2009) *"export_fig"* [online] Available at: http://www.mathworks.co.uk/matlabcentral/fileexchange/23629-exportfig [Accessed 20/03/2014]

[17] Arfken, G. and Weber, H. *"Mathematical Methods for Physicists"*, 4th Ed., Academic Press, (1995)

[18] Jackson, J. *"Classical Electrodynamics"*, 3rd Ed., Wiley, (1998)

[19] Goodman, J. *"Introduction to Fourier Optics"*, 3rd Ed., Roberts & Co., (2005)

[20] Kirchoff, G. *"Zur Theorie der Lichtstrahlen"*, Weidemann Ann. (2) **18**, pp. 663, (1883)

[21] Marion, J. and Heald, M. *"Classical Electromagnetic Radiation"*, 2nd Ed., Academic Press, (1980)

[22] Morse, P. and Feshbach, H. *"Methods of Theoretical Physics"*, McGraw-Hill, (1953)

[23] Mertz, J. *"Introduction to Optical Microscopy"*, Roberts & Company Publishers, (2010)

[24] Goodman, J. *"Statistical Optics"*, Wiley, (2000)

[25] Walther, A. *"Radiometry and coherence"*, J. Opt. Soc. Am. **58**, pp. 1256 – 1259, (1968)

[26] Walther, A. *"Propagation of the generalized radiance through lenses"*, J. Opt. Soc. Am. **68**, pp. 1606 – 1610, (1978)

[27] Bracewell, R. *"The Fourier Transform and its Applications"*, McGraw-Hill, (1965)

[28] Hecht, E. *"Optics"*, Addison – Wesley, (2002)

[29] Born, M. and Wolf, E. *"Principles of Optics"*, 6th Ed., Cambridge University Press, (1980)

[30] Hawkes, P. *et al. "Science of Microscopy: Volume II"*, Springer, (2007)

[31] Schwinder, J. *et al. "Digital wave-front measuring interferometry: some systematic error sources"*, Appl. Opt. **22**, pp. 3421 – 3432, (1983)

9. Appendices

Appendix A: Matlab computational code

```
%% X-ray SIM Script with TWINMIC TXM Parameters %%
% This script simulates the TWIN-MIC TXM system located at the Elettra
% synchrotron near Trieste, Italy. The parameters used are those
% characteristic of TWIN-MIC, and the code uses Fourier optics theory to
% construct the simulation. A thick sample is imaged, corresponding to
% three transmission objects read in as .jpg files, located at some
% equidistant spacing, with one centred on the focal plane.

%% Script Initialisation %%

clear all
close all
clc
set(0,'DefaultTextInterpreter', 'latex');

%% Parameter Initialisation %%
% This section establishes the defining parameters and dimensions of the
% TWIN-MIC TXM which is being simulated

lambda = 2.49E-9; % wavelength of illumination/m
k = 1/lambda; % wavenumber of illumination/m^-1
f1 = 6E-3; % focal length of CZP/m
D1 = 500E-6; % outer diameter of CZP/m
D1a = 220E-6; % inner diameter of CZP/m
z1 = 52E-3; % grating to CZP distance/m
z2 = 6.75E-3; % CZP to sample distance/m
magnification_1 = -z2/z1; % maginification of CZP
f2 = 3E-3; % focal length of OZP/m
D2 = 250E-6; % outer diameter of OZP/m
D2a = 110E-6; % inner diameter of OZP/m
z3 = 3E-3; % sample to OZP distance/m
z4 = 4; % OZP to CCD distance/m
magnification_2 = -z4/z3; % maginification of OZP
magnification = magnification_1*magnification_2; % total system
magnification

%% Fringe Illumination Generation %%
% This section establishes the illumination (fringe object) for four
% translations of the grating, determined by four well-defined phases

period_number = 15; % number of periods of fringe pattern
period_width = 940E-9; % width of fringe period/m
x0_width = period_number*period_width; % fringe object x width
y0_width = period_number*period_width; % fringe object y width
sampling_number = 512; % number of position samples in each dimension of
fringe pattern
x0_unpadded = [-x0_width/2:x0_width/(sampling_number - 1):x0_width/2]; %
unpadded sampling x co-ordinates
y0_unpadded = [-y0_width/2:y0_width/(sampling_number - 1):y0_width/2]; %
unpadded sampling y co-ordinates

% Phase shifts are for four-step SIM algorithm, with phi incrementing in
% accordance with phi = (2pi)K/N, where N = 4, K = {0,1,2,3}
phi_1 = 0*((2*pi())/4); % 1st phase shift of fringe pattern
phi_2 = 1*((2*pi())/4); % 1st phase shift of fringe pattern
phi_3 = 2*((2*pi())/4); % 1st phase shift of fringe pattern
```

```
phi_4 = 3*((2*pi())/4); % 1st phase shift of fringe pattern

% Sinudoial fringe patterns with well-defined phase translations in
% x-direction are established
cos_wave_x_1 = 0.5.*(1 +
cos(period_number.*2.*pi().*(x0_unpadded./(x0_width)) + phi_1)); %
sinusoidal fringe pattern phase 0
cos_wave_x_2 = 0.5.*(1 +
cos(period_number.*2.*pi().*(x0_unpadded./(x0_width)) + phi_2)); %
sinusoidal fringe pattern phase pi/2
cos_wave_x_3 = 0.5.*(1 +
cos(period_number.*2.*pi().*(x0_unpadded./(x0_width)) + phi_3)); %
sinusoidal fringe pattern phase pi
cos_wave_x_4 = 0.5.*(1 +
cos(period_number.*2.*pi().*(x0_unpadded./(x0_width)) + phi_4)); %
sinusoidal fringe pattern phase 3pi/2
cos_wave_y = ones(length(y0_unpadded),1); % uniform illumination in y-
direction

% 2D Illumination profiles are generated
cos_wave_a_1 = (cos_wave_y*cos_wave_x_1); % 2D illumination pattern phase 0
cos_wave_a_2 = (cos_wave_y*cos_wave_x_2); % 2D illumination pattern phase
pi/2
cos_wave_a_3 = (cos_wave_y*cos_wave_x_3); % 2D illumination pattern phase
pi
cos_wave_a_4 = (cos_wave_y*cos_wave_x_4); % 2D illumination pattern phase
3pi/2

pad_amount = 0.5.*sampling_number; % padding element number for positiive
and negative co-ordinate directions

% Intermediate zero-padded illumination profiles
cos_wave_b_1 = padarray(cos_wave_a_1,[pad_amount pad_amount],'both'); %
padded fringe illumination phase 0
cos_wave_b_2 = (padarray(cos_wave_a_2,[pad_amount pad_amount],'both')); %
padded fringe illumination phase pi/2
cos_wave_b_3 = (padarray(cos_wave_a_3,[pad_amount pad_amount],'both')); %
padded fringe illumination phase pi
cos_wave_b_4 = (padarray(cos_wave_a_4,[pad_amount pad_amount],'both')); %
padded fringe illumination phase 3pi/2

rot_angle = 10; % Arbitrary array rotation angle to prevent aliasing

% Final zero-padded rotated illumination profiles
cos_wave_c_1 = imrotate(cos_wave_b_1,rot_angle);
cos_wave_c_2 = imrotate(cos_wave_b_2,rot_angle);
cos_wave_c_3 = imrotate(cos_wave_b_3,rot_angle);
cos_wave_c_4 = imrotate(cos_wave_b_4,rot_angle);

ratio = length(cos_wave_1c(:,1))/length(cos_wave_1a(:,1)).*((2.*pad_amount
+ sampling_number)/(sampling_number)); % ratio of element number for
padded/unpadded co-ordinate arrays

x0 = [((-x0_width/2)*ratio):((x0_width*ratio)/(rot_ratio.*(2.*pad_amount +
sampling_number) - 1)):((x0_width/2)*ratio)]; % final fringe pattern x co-
ordinates
y0 = [((-y0_width/2)*ratio):((y0_width*ratio)/(rot_ratio.*(2.*pad_amount +
sampling_number) - 1)):((y0_width/2)*ratio)]; % final fringe pattern y co-
ordinates
[X0,Y0] = meshgrid(x0,y0); % meshgrid of x,y co-ordinates
```

```
%% CZP Reciprocal Space co-ordinates generation %%

del_x0 = x0(2) - x0(1); % increment in fringe pattern x co-ordinates
del_y0 = y0(2) - y0(1); % increment in fringe pattern y co-ordinates
M_x = length(x0) - 1; % number of x co-ordinate increments
M_y = length(y0) - 1; % number of y co-ordinate increments
del_q1_x = 1./(M_x.*del_x0); % increment in reciprocal space CZP x co-
ordinates
del_q1_y = 1./(M_y.*del_y0); % increment in reciprocal space CZP y co-
ordinates
q1_x = [-(M_x.*del_q1_x)/2:del_q1_x:(M_x.*del_q1_x)/2]; % reciprocal space
CZP x co-ordinates
q1_y = [-(M_y.*del_q1_y)/2:del_q1_y:(M_y.*del_q1_y)/2]; % reciprocal space
CZP y co-ordinates
del_x1 = lambda.*z1.*del_q1_x; % increment in real space CZP x co-ordinates
del_y1 = lambda.*z1.*del_q1_y; % increment in real space CZP y co-ordinates
x1 = [-(M_x.*del_x1)/2:del_x1:(M_x.*del_x1)/2]; % real space CZP x co-
ordinates
y1 = [-(M_y.*del_y1)/2:del_y1:(M_y.*del_y1)/2]; % real space CZP y co-
ordinates
[X1,Y1] = meshgrid(x1,y1); % meshgrid of x,y CZP co-ordinates
R1 = (X1.^2 + Y1.^2).^0.5; % radial co-ordinates in intermediate plane

%% CZP CTF Generation %%

CZP_CTF = zeros(length(R1(:,1)),length(R1(1,:))); % CZP CTF initialisation
for i = [1:length(R1(:,1))]; % for loop executes to implement rect function
    for j = [1:length(R1(1,:))];
       if abs(R1(i,j)) <= D1/2 && abs(R1(i,j)) >= D1a/2;
           CZP_CTF(i,j) = 1;
       end
    end
end

%% Sample Image field co-ordinates generation %%

x2 = magnification_1.*x0; % sample x co-ordinate equal to scaled object x
co-ordinate
y2 = magnification_1.*y0; % sample y co-ordinate equal to scaled object y
co-ordinate
[X2,Y2] = meshgrid(x2,y2); % meshgrid of sample x,y co-ordinates
R2 = (X2.^2 + Y2.^2).^(0.5); % radial co-ordinates in sample plane
del_q2xprime = 1./(x2(2) - x2(1)); % increment in reciprocal space sample x
co-ordinates
del_q2yprime = 1./(y2(2) - y2(1)); % increment in reciprocal space sample y
co-ordinates
q2xprime = [-del_q2xprime/2:del_q2xprime/(length(x2) - 1):del_q2xprime/2];
% reciprocal space sample x co-ordinates
q2yprime = [-del_q2yprime/2:del_q2yprime/(length(y2) - 1):del_q2yprime/2];
% reciprocal space sample y co-ordinates
[Q2x,Q2y] = meshgrid(q2xprime,q2yprime); % meshgrid of reciprocal space co-
ordinates
Q2 = (Q2x.^2 + Q2y.^2).^(0.5); % reciprocal space sample radial co-
ordinates

%% Defocus Parameters %%

z_d_1 = -6E-6; % upsteam defocus value
z_d_2 = -1*z_d_1; % inverse upstream defocus value
```

```
z_d_3 = 6E-6; % downstream defocus value
z_d_4 = -1*z_d_3; % inverse downstream defocus value

H2_a = exp(-1i.*pi().*lambda.*z_d_1.*(Q2.^2)); % upstream defocus operator
H2_b = exp(-1i.*pi().*lambda.*z_d_2.*(Q2.^2)); % inverse upstream defocus
operator
H2_c = exp(-1i.*pi().*lambda.*z_d_3.*(Q2.^2)); % downstream defocus
operator
H2_d = exp(-1i.*pi().*lambda.*z_d_4.*(Q2.^2)); % inverse downstream defocus
operator

pad_amount_1 = round((length(x2(1,:))-1024)/2) - 1; % 1st pad amount to
transmission objects

A_shape_a = padarray(flipud(imread('A_shape.bmp')),[pad_amount_1
pad_amount_1],'both'); % A shape object is read in and padded
pad_amount_2 = length(x2(1,:)) - length(A_shape_a(1,:)); % final pad amount
for transmission objects
A_shape = 0.5.*(padarray(A_shape_a,[pad_amount_2 pad_amount_2],'pre') + 1);
% A shape is padded and shifted to 0.5 transmission
B_shape_a = padarray(flipud(imread('B_shape.bmp')),[pad_amount_1
pad_amount_1],'both'); % B shape object is read in and padded
B_shape = 0.5.*(padarray(B_shape_a,[pad_amount_2 pad_amount_2],'pre') + 1);
% B shape is padded and shifted to 0.5 transmission
C_shape_a = padarray(flipud(imread('C_shape.bmp')),[pad_amount_1
pad_amount_1],'both'); % C shape object is read in and padded
C_shape = 0.5.*(padarray(C_shape_a,[pad_amount_2 pad_amount_2],'pre') + 1);
% C shape is padded and shifted to 0.5 transmission

%% OZP reciprocal space co-ordinates generation %%

del_x2 = x2(2) - x2(1); % increment in sample x co-ordinates
del_y2 = y2(2) - y2(1); % increment in sample y co-ordinates
del_q3_x = 1./(M_x.*del_x2); % increment in reciprocal space OZP x co-
ordinates
del_q3_y = 1./(M_y.*del_y2); % increment in reciprocal space OZP y co-
ordinates
q3_x = [-(M_x.*del_q3_x)./2:del_q3_x:(M_x.*del_q3_x)./2]; % reciprocal
space OZP x co-ordinates
q3_y = [-(M_y.*del_q3_y)./2:del_q3_y:(M_y.*del_q3_y)./2]; % reciprocal
space OZP y co-ordinates
del_x3 = lambda.*z3.*del_q3_x; % increment in real space OZP x co-ordinates
del_y3 = lambda.*z3.*del_q3_y; % increment in real space OZP y co-ordinates
x3 = [-(M_x.*del_x3)./2:del_x3:(M_x.*del_x3)./2]; % real space OZP x co-
ordinates
y3 = [-(M_y.*del_y3)./2:del_y3:(M_y.*del_y3)./2]; % real space OZP y co-
ordinates
[X3,Y3] = meshgrid(x3,y3); % meshgrid of OZP x,y co-ordinates
R3 = (X3.^2 + Y3.^2).^0.5; % radial co-ordinates in OZP plane

%% OZP CTF Generation %%

OZP_CTF = zeros(length(R3(:,1)),length(R3(1,:))); % OZP CTF initialisation
for i = [1:length(R3(:,1))]; % for loop executes to implement rect function
    for j = [1:length(R3(1,:))];
       if abs(R3(i,j)) <= D2/2 && abs(R3(i,j)) >= D2a/2;
           OZP_CTF(i,j) = 1;
       end
    end
end
```

```
%% CCD Image field Calculation %%

x4 = magnification_2.*x2; % CCD x co-ordinate equal to scaled sample x co-
ordinate
y4 = magnification_2.*y2; % CCD y co-ordinate equal to scaled sample y co-
ordinate

%% Final image intensity generation %%

I_CCD_1 = zeros(length(x4),length(x4)); % intensity profile initialised for
phase phi = 0
I_CCD_2 = zeros(length(x4),length(x4)); % intensity profile initialised for
phase phi = pi/2
I_CCD_3 = zeros(length(x4),length(x4)); % intensity profile initialised for
phase phi = pi
I_CCD_4 = zeros(length(x4),length(x4)); % intensity profile initialised for
phase phi = 3pi/2

phase = [0:(2*pi()/(sampling_number - 1)):(2*pi())]; % 2pi phase ramp

for zl = [-17:17]; % phase ramp x gradients
    for jw = [-17:17]; % phase ram y gradients
        phase_xya = transpose(exp(1i.*(zl).*phase))*exp(1i.*(jw).*phase); %
unpadded phase ramp array
        phase_xyb = padarray(phase_xya,[pad_amount pad_amount],'both'); %
padded phase ramp array
        phase_xy = imrotate(phase_xyb,(rot_angle)); % padded rotated phase
ramp array

        cos_wave_1 = phase_xy.*cos_wave_1c; % phase-ramped source wave for
phase phi = 0
        cos_wave_2 = phase_xy.*cos_wave_2c; % phase-ramped source wave for
phase phi = pi/2
        cos_wave_3 = phase_xy.*cos_wave_3c; % phase-ramped source wave for
phase phi = pi
        cos_wave_4 = phase_xy.*cos_wave_4c; % phase-ramped source wave for
phase phi = 3pi/2

        diffraction_pattern_1_1 = fftshift(fft2(cos_wave_1)).*CZP_CTF; %
source wave CZP-limited diffraction pattern for phase phi = 0
        diffraction_pattern_2_1 = fftshift(fft2(cos_wave_2)).*CZP_CTF; %
source wave CZP-limited diffraction pattern for phase phi = pi/2
        diffraction_pattern_3_1 = fftshift(fft2(cos_wave_3)).*CZP_CTF; %
source wave CZP-limited diffraction pattern for phase phi = pi
        diffraction_pattern_4_1 = fftshift(fft2(cos_wave_4)).*CZP_CTF; %
source wave CZP-limited diffraction pattern for phase phi = 3pi/2

        E_sample_1_a = (ifft2(diffraction_pattern_1_1.*H2_a)).*A_shape; %
sample wave upsteam for phase phi = 0
        E_sample_1_b = (ifft2((fft2(E_sample_1_a)).*H2_b)).*B_shape; %
sample wave A transmitted for phase phi = 0
        E_sample_1_c = (ifft2((fft2(E_sample_1_b)).*H2_c)).*C_shape; %
sample wave downstream A, B transmitted for phase phi = 0
        E_sample_1 = (ifft2((fft2(E_sample_1_c)).*H2_d)); % sample wave A,
B, C transmitted for phase phi = 0

        E_sample_2_a = (ifft2(diffraction_pattern_2_1.*H2_a)).*A_shape; %
sample wave upsteam for phase phi = pi/2
```

```
        E_sample_2_b = (ifft2((fft2(E_sample_2_a)).*H2_b)).*B_shape; %
sample wave A transmitted for phase phi = pi/2
        E_sample_2_c = (ifft2((fft2(E_sample_2_b)).*H2_c)).*C_shape; %
sample wave downstream A, B transmitted for phase phi = pi/2
        E_sample_2 = (ifft2((fft2(E_sample_2_c)).*H2_d)); % sample wave A,
B, C transmitted for phase phi = pi/2

        E_sample_3_a = (ifft2(diffraction_pattern_3_1.*H2_a)).*A_shape; %
sample wave upsteam for phase phi = pi
        E_sample_3_b = (ifft2((fft2(E_sample_3_a)).*H2_b)).*B_shape; %
sample wave A transmitted for phase phi = pi
        E_sample_3_c = (ifft2((fft2(E_sample_3_b)).*H2_c)).*C_shape; %
sample wave downstream A, B transmitted for phase phi = pi
        E_sample_3 = (ifft2((fft2(E_sample_3_c)).*H2_d)); % sample wave A,
B, C transmitted for phase phi = pi

        E_sample_4_a = (ifft2(diffraction_pattern_4_1.*H2_a)).*A_shape; %
sample wave upsteam for phase phi = 3pi/2
        E_sample_4_b = (ifft2((fft2(E_sample_4_a)).*H2_b)).*B_shape; %
sample wave A transmitted for phase phi = 3pi/2
        E_sample_4_c = (ifft2((fft2(E_sample_4_b)).*H2_c)).*C_shape; %
sample wave downstream A, B transmitted for phase phi = 3pi/2
        E_sample_4 = (ifft2((fft2(E_sample_4_c)).*H2_d)); % sample wave A,
B, C transmitted for phase phi = 3pi/2

        diffraction_pattern_1_2 = (fft2(E_sample_1)).*OZP_CTF; % sample
wave OZP-limited diffraction pattern for phase phi = 0
        diffraction_pattern_2_2 = (fft2(E_sample_2)).*OZP_CTF; % sample
wave OZP-limited diffraction pattern for phase phi = pi/2
        diffraction_pattern_3_2 = (fft2(E_sample_3)).*OZP_CTF; % sample
wave OZP-limited diffraction pattern for phase phi = pi
        diffraction_pattern_4_2 = (fft2(E_sample_4)).*OZP_CTF; % sample
wave OZP-limited diffraction pattern for phase phi = 3pi/2

        E_CCD_1 = ifft2(diffraction_pattern_1_2); % CCD wave for phase phi
= 0
        E_CCD_2 = ifft2(diffraction_pattern_2_2); % CCD wave for phase phi
= pi/2
        E_CCD_3 = ifft2(diffraction_pattern_3_2); % CCD wave for phase phi
= pi
        E_CCD_4 = ifft2(diffraction_pattern_4_2); % CCD wave for phase phi
= 3pi/2

        I_CCD_1 = I_CCD_1 + abs(E_CCD_1).^2; % intensity profile sums
independent phase ramps for phase phi = 0
        I_CCD_2 = I_CCD_2 + abs(E_CCD_2).^2; % intensity profile sums
independent phase ramps for phase phi = pi/2
        I_CCD_3 = I_CCD_3 + abs(E_CCD_3).^2; % intensity profile sums
independent phase ramps for phase phi = pi
        I_CCD_4 = I_CCD_4 + abs(E_CCD_4).^2; % intensity profile sums
independent phase ramps for phase phi = 3pi/2
    end
end

%% SIM image generation %%

% SIM image generated using four-step algorithm using intensities for phase
% shifts phi = 0, pi/2, pi, 3pi/2
I_SIM = abs(0.25.*((I_CCD_1.*exp(1i.*phi_1)) + (I_CCD_2.*exp(1i.*phi_2)) +
(I_CCD_3.*exp(1i.*phi_3)) + (I_CCD_4.*exp(1i.*phi_4))));
```

```
%% Figure Plotting %%

% SIM image is plotted as false-colour map
figure
contourf(abs(I_SIM),'LineColor','none')
colormap('jet')
axis image
set(gca,'XTick',[1 1189])
set(gca,'YTick',[1 1189])
set(gca,'XTickLabel',{'-2.9E-3','2.9E-3'})
set(gca,'YTickLabel',{'-2.9E-3','2.9E-3'})
set(gcf,'color','w')
export_fig CCD_Plane_ABC_ISIM_6um -pdf

% Intensity for phase phi = 0 is plotted as false-colour map
figure
contourf(abs(I_CCD_1),'LineColor','none')
colormap('jet')
axis image
set(gca,'XTick',[1 1189])
set(gca,'YTick',[1 1189])
set(gca,'XTickLabel',{'-2.9E-3','2.9E-3'})
set(gca,'YTickLabel',{'-2.9E-3','2.9E-3'})
set(gcf,'color','w')
export_fig CCD_Plane_I1_6um -pdf

% Intensity for phase phi = pi/2 is plotted as false-colour map
figure
contourf(abs(I_CCD_2),'LineColor','none')
colormap('jet')
axis image
set(gca,'XTick',[1 1189])
set(gca,'YTick',[1 1189])
set(gca,'XTickLabel',{'-2.9E-3','2.9E-3'})
set(gca,'YTickLabel',{'2.9E-3','-2.9E-3'})
set(gcf,'color','w')
export_fig CCD_Plane_ABC_I2_6um -pdf

% Intensity for phase phi = pi is plotted as false-colour map
figure
contourf(abs(I_CCD_3),'LineColor','none')
colormap('jet')
axis image
set(gca,'XTick',[1 1189])
set(gca,'YTick',[1 1189])
set(gca,'XTickLabel',{'-2.9E-3','2.9E-3'})
set(gca,'YTickLabel',{'2.9E-3','-2.9E-3'})
set(gcf,'color','w')
export_fig CCD_Plane_ABC_I3_6um -pdf

% Intensity for phase phi = 3pi/2 is plotted as false-colour map
figure
contourf(abs(I_CCD_4),'LineColor','none')
colormap('jet')
axis image
set(gca,'XTick',[1 1189])
set(gca,'YTick',[1 1189])
set(gca,'XTickLabel',{'-2.9E-3','2.9E-3'})
set(gca,'YTickLabel',{'2.9E-3','-2.9E-3'})
```

```
set(gcf,'color','w')
export_fig CCD_Plane_ABC_I4_6um -pdf
```